

Confronting 2D delayed-detonation models with light curves and spectra of Type Ia supernovae

Stéphane Blondin,^{1*} Daniel Kasen,^{2,3} Friedrich K. Röpkke,^{4,5} Robert P. Kirshner⁶
and Kaisey S. Mandel⁶

¹*Centre de Physique des Particules de Marseille (CPPM), Université Aix-Marseille, CNRS/IN2P3, 163 avenue de Luminy, 13288 Marseille Cedex 9, France*

²*Department of Physics, University of California at Berkeley, 366 LeConte, Berkeley, CA 94720, USA*

³*Nuclear Science Division, Lawrence Berkeley National Laboratory, Berkeley, CA 94720, USA*

⁴*Universität Würzburg, Am Hubland, D-97074 Würzburg, Germany*

⁵*Max-Planck-Institut für Astrophysics, Karl-Schwarzschild-Strasse 1, D-85741 Garching, Germany*

⁶*Harvard-Smithsonian Center for Astrophysics, 60 Garden Street, Cambridge, MA 02138, USA*

Accepted 2011 June 28. Received 2011 June 27; in original form 2011 April 18

ABSTRACT

We compare models for Type Ia supernova (SN Ia) light curves and spectra with an extensive set of observations. The models come from a recent survey of 44 two-dimensional delayed-detonation models computed by Kasen, Röpkke & Woosley (2009), each viewed from multiple directions. The data include optical light curves of 251 SNe Ia, some of which have near-infrared observations, and 2231 low-dispersion spectra from the Center for Astrophysics, plus data from the literature. These allow us to compare a wide range of SN Ia models with observations for a wide range of luminosities and decline rates. The analysis uses standard techniques employed by observers, including MLCS2k2, SALT2, and SNooPy for light-curve analysis, and the Supernova Identification (SNID) code of Blondin & Tonry for spectroscopic comparisons to assess how well the models match the data. The ability to use the tools developed for observational data directly on the models marks a significant step forward in the realism of the models. We show that the models that match observed spectra best lie systematically on the observed width-luminosity relation. Conversely, we reject six models with highly asymmetric ignition conditions and a large amount ($\gtrsim 1 M_{\odot}$) of synthesized ^{56}Ni that yield poor matches to observed SN Ia spectra. More subtle features of the comparison include the general difficulty of the models to match the U -band flux at early times, caused by a hot ionized ejecta that affect the subsequent redistribution of flux at longer wavelengths. The models have systematically higher velocities than the observed spectra at maximum light, as inferred from the Si II $\lambda 6355$ line. We examine ways in which the asymptotic kinetic energy of the explosion affects both the predicted velocity and velocity gradient in the Si II and Ca II lines. Models with an asymmetric distribution of ^{56}Ni are found to result in a larger variation of photometric and spectroscopic properties with viewing angle, regardless of the initial ignition setup. We discuss more generally whether highly anisotropic ignition conditions are ruled out by observations, and how detailed comparisons between models and observations involving both light curves and spectra can lead to a better understanding of SN Ia explosion mechanisms.

Key words: supernovae: general

1 INTRODUCTION

Type Ia supernovae (SNe Ia) play a major role in many astrophysical phenomena. They produce a large fraction of iron in the universe (e.g., Truran & Cameron 1971), heat the interstellar medium (e.g., Ciotti et al. 1991), and form an endpoint of binary star evolution (e.g., Iben & Tutukov 1984). SNe Ia provide the most reliable

and precise cosmological distances to establish the acceleration of cosmic expansion (Riess et al. 1998; Perlmutter et al. 1999).

Despite their astrophysical importance, however, they remain enigmatic objects. There is a general consensus that they result from the thermonuclear disruption of a carbon-oxygen white dwarf (WD) star (Hoyle & Fowler 1960) approaching the Chandrasekhar mass ($M_{\text{Ch}} \approx 1.4 M_{\odot}$), either through accretion from a non-degenerate binary companion (the “single-degenerate” scenario), or through merger with another WD (the “double-degenerate” scenario; Iben & Tutukov 1984; Webbink 1984). Which of these two

* E-mail: blondin@cppm.in2p3.fr

possibilities constitutes the dominant (or sole) progenitor channel for SNe Ia is still debated (see Howell 2010 for a recent review).

The explosion mechanism itself is also largely unknown (see Hillebrandt & Niemeyer 2000 for a review). In the preferred “delayed-detonation” model (Khokhlov 1991), the burning starts as a turbulent subsonic deflagration near the WD center and transitions to a supersonic detonation near its surface. The deflagration pre-expands the WD so that the subsequent detonation does not burn the entire star to nuclear statistical equilibrium (NSE) material (including ^{56}Ni to power the light curve), but instead synthesizes appropriate fractions of high-velocity ($\sim 10000 \text{ km s}^{-1}$) intermediate-mass elements (IME; such as Mg, Si, S, Ca, etc.) needed to reproduce the observed spectra. The first simulations were carried out in 1D, but recent studies show that multi-dimensional simulations are needed to capture hydrodynamical instabilities (e.g., Gamezo, Khokhlov & Oran 2005; Röpke & Niemeyer 2007) and to provide a physical basis for the transition from deflagration to detonation. (e.g., Woosley 2007; Röpke 2007; Woosley et al. 2009).

The empirical relation between the peak luminosity and the width of the light-curve (the so-called width-luminosity relation, or WLR; Pskovskii 1977; Phillips 1993), instrumental to the use of SNe Ia as distance indicators, can be physically interpreted in terms of (1) varying opacity with the amount of synthesized ^{56}Ni (Hoefflich & Khokhlov 1996), (2) varying mass of the progenitor WD (Pinto & Eastman 2000a), or (3) the III \rightarrow II (i.e. doubly- to singly-ionized) recombination timescale of iron-group elements in the SN atmosphere (Kasen & Woosley 2007). More detailed calculations are also needed to explain the observed scatter in the WLR.

In a recent paper, Kasen, Röpke & Woosley (2009) (hereafter KRW09) conducted a 2D survey of delayed-detonation models, in which they varied the radial/angular distribution and number of ignition points in a Chandrasekhar-mass C+O WD star, as well as the criterion for deflagration-to-detonation transition. By synthesizing light curves and spectra for different viewing angles, they were able to broadly reproduce both the observed width-luminosity relation (for all but subluminescent SNe Ia) and its scatter, illustrating the importance of multi-dimensional computations to reproduce observed trends in SN Ia properties. Furthermore, they showed that variations in the metallicity of the progenitor WD affect both the slope and normalization of the WLR, and that ignoring these effects could potentially lead to systematic overestimates of $\sim 2\%$ on distance determinations to SNe Ia.

To study such subtle effects, one must ensure the models reproduce all observed trends in some detail, and not just the width-luminosity relation. This is precisely what we set out to do in the present study, where we conduct an extensive analysis of the delayed-detonation models of KRW09 through a detailed and direct comparison with observations of SNe Ia. We present the models and data in § 2, and our methods for quantitatively evaluating each model in § 3. We then proceed to a detailed comparison of their photometric (§ 4) and spectroscopic (§ 5) properties with actual data. We discuss whether explosion models with asymmetric ignition conditions are ruled out by observations in § 6, and conclude in § 7.

2 MODELS AND DATA

2.1 2D delayed-detonation models from KRW09

Kasen, Röpke & Woosley (2009) simulated 44 axisymmetric two-

dimensional delayed-detonation explosions in a non-rotating spherical Chandrasekhar-mass WD star composed of equal mass fractions of carbon and oxygen. They varied both the radial/angular distributions and number of ignition points used to trigger the deflagration (which control the level of asymmetry of the explosion), as well as the criterion for the transition to a detonation (termed “dc”, and parameterized via the critical Karlovitz number, which controls the level of turbulence in the combustion). We refer the reader to KRW09 for more information on the initial conditions for each model, but note that these were chosen *a priori*, and not tuned to match the range of observed SN Ia properties.

Table 1 gives the asymptotic kinetic energy (E_{kin}), abundances, peak bolometric luminosities ($L_{\text{bol,peak}}$) and $\Delta m_{15}(B)$ ¹ decline-rate ranges for all the models of KRW09. Models with an isotropic (anisotropic) distribution of ignition points are labeled DD2D_iso (DD2D_asym). One exception concerns the DD2D_asym_01 model series, which in fact has an isotropic distribution of ignition points. The number that follows (01–08) corresponds to a particular ignition setup, and the criterion for deflagration-to-detonation transition (dc) is also included in the model name (see Tables 1 & 2 in KRW09). The models span a large range in mass of synthesized ^{56}Ni ($0.29\text{--}1.10 M_{\odot}$) and decline rate parameters $\Delta m_{15}(B)$ ($0.74\text{--}1.57 \text{ mag}$). The models are unable to reproduce rapidly-declining SNe Ia such as the subluminescent SN 1991bg (see Taubenberger et al. 2008 for a discussion on this class of objects). Model DD2D_iso_01_dc4 was accidentally omitted in the radiative transfer calculations, but this does not affect the results presented in this paper. We do not study the impact of metallicity variations in the progenitor WD star (between $1/3$ to $3\times$ solar; see KRW09). We selected eight models for detailed analysis, and rejected six models based on their spectra (see § 3.3). These are marked as “subset” and “rejected” in Table 1.

The models were evolved hydrodynamically until ~ 100 s past ignition, at which point the ejecta had reached a phase of homologous expansion (velocity proportional to radius). Figure 1 shows the total mass density distribution for models DD2D_iso_06_dc2 (*top left*) and DD2D_asym_01_dc3 (*bottom left*). The white contours correspond to a ^{56}Ni mass fraction of 10^{-3} . The ^{56}Ni distribution is roughly symmetric about ($z = 0$) in model DD2D_iso_06_dc2, while it is strongly skewed toward $z > 0$ in model DD2D_asym_01_dc3, this despite the isotropic distribution of ignition points in both models.

A crude nuclear network was used to determine the distributions of radioactive ^{56}Ni , stable iron-group elements (IGE), and intermediate-mass elements (IME; such as Mg, Si, S, and Ca), but detailed abundances of all important chemical species were determined based on a more elaborate nuclear network applied to a representative model (DD2D_iso_06_dc2²) using 12800 tracer particles (see Travaglio et al. 2004) and interpolated accordingly for the other models. The nucleosynthetic yields are thus subject to some uncertainty which can impact the derived observables.

The abundances were then remapped on a 64×128 cylindrical grid with a velocity cutoff of $\sim 25000 \text{ km s}^{-1}$ for the radiative transfer calculations. These were done with the time-dependent Monte Carlo radiative transfer code SEDONA (Kasen, Thomas & Nugent 2006) using 10^8 photon packets and 13 chemical species (ionization stages I–V): C, O, Na, Mg, Si, S, Ar,

¹ the difference in B -band magnitude between maximum light and 15 d after maximum; Phillips 1993)

² and not DD2D_iso_06_dc1, as stated by KRW09.

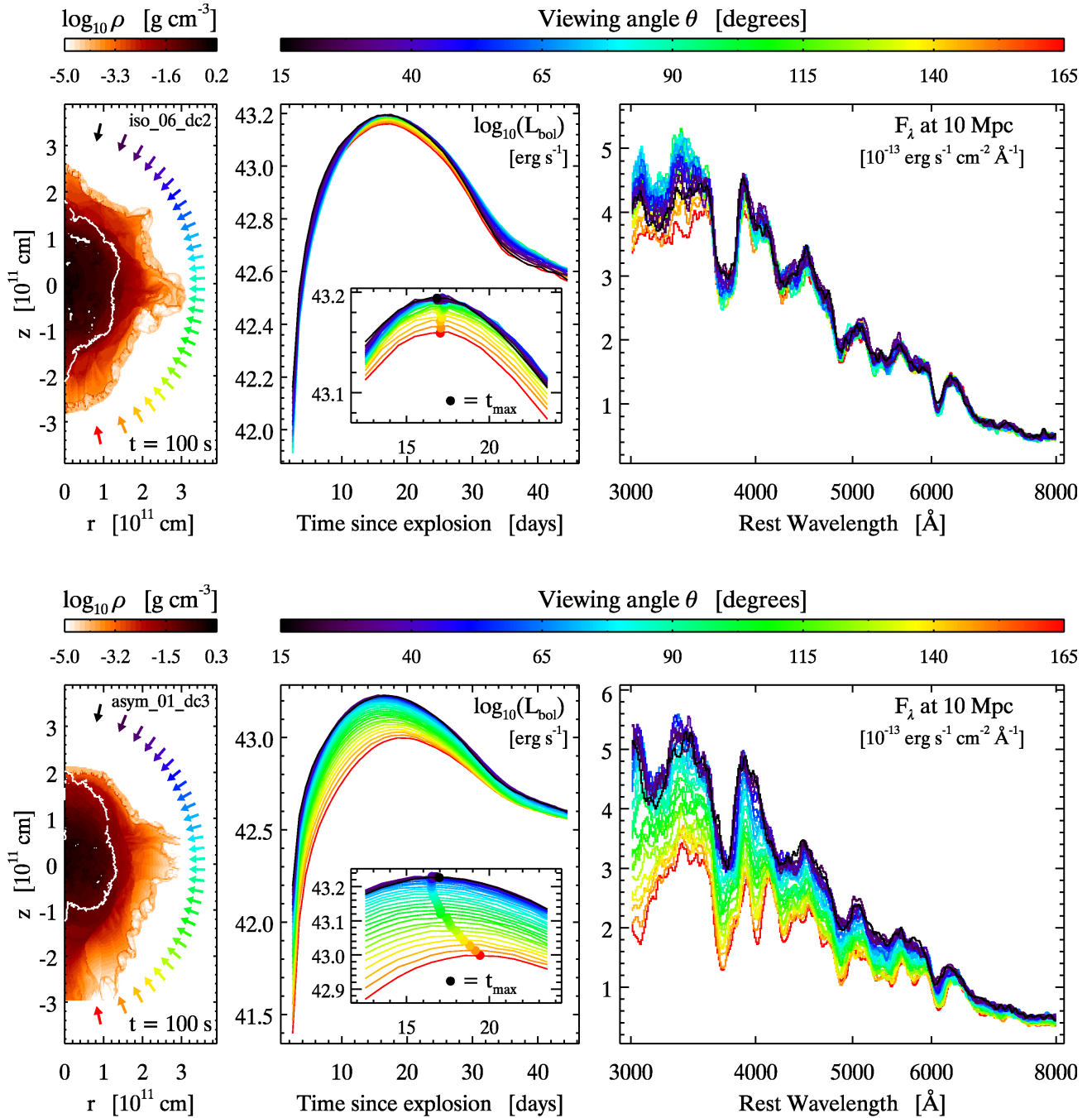


Figure 1. *Top left:* Total mass density distribution at $t = 100$ s for model DD2D_iso_06_dc2. The ejecta are in homologous expansion, and 10^{11} cm in (r, z) corresponds to 10^4 km s⁻¹ in (v_r, v_z) . The white contours correspond to a ⁵⁶Ni mass fraction of 10^{-3} . The arrows denote the 30 different viewing angles. *Top center:* Bolometric light curves as a function of viewing angle. The inset shows the maximum-light region, with filled circles corresponding to the time of bolometric maximum. *Top right:* Optical spectra (3000–8000 Å) as a function of viewing angle. *Bottom row:* Same as above but for model DD2D_asym_01_dc3.

Ca, Ti, Cr, Fe, Co, and Ni. Local thermodynamic equilibrium (LTE) was assumed for the atomic level populations, although non-LTE effects in the radiation field were treated approximately through an equivalent two-level atom formalism. The photon packets were collected into 30 separate viewing angle bins ($15^\circ \lesssim \theta \lesssim 165^\circ$), offering a 2D view of the explosion. The bins are equally spaced in $\cos \theta$, so that each bin subtends the same solid angle and has an equal probability of being observed. The arrows in the left panels of Fig. 1 denote the viewing angles considered by KRW09. The

limited number of photon packets and the large number of viewing angles results in moderate S/N in individual angle-dependent light curves and spectra (typically $S/N \approx 15$ – 20 per 10 Å in B and V at maximum light). The velocity cutoff of ~ 25000 km s⁻¹ also limits the formation of high-velocity absorption features, which are common in early-time SN Ia spectra (e.g. Mazzali et al. 2005).

Spectra were computed between 2.5 d and 44.5 d after explosion (i.e. between -17 (-15) d and $+25$ ($+27$) d from B -band maximum for a 19.5 (17.5) d rise time) in 1 d steps. At later times, non-

LTE effects and non-thermal excitation by fast electrons become increasingly important (e.g., Kozma & Fransson 1992) and the radiative transfer calculations are less reliable³. The mass fraction of (unburnt) carbon dominates over all other intermediate-mass elements at $v \gtrsim 16000\text{--}21000 \text{ km s}^{-1}$, but we are unable to study the presence of corresponding spectral lines (e.g. C II $\lambda 6580$) in the early-time spectra due to limited signal in the Monte Carlo spectra. The total mass of (unburnt) carbon is $\lesssim 0.04 M_{\odot}$ for all models.

Figure 1 shows the variation of bolometric light curves (*middle panels*) and optical spectra (*right panels*) with viewing angle for models DD2D_iso_06_dc2 (*top*) and DD2D_asym_01_dc3 (*bottom*). In model DD2D_iso_06_dc2, the peak bolometric luminosity varies by $< 10\%$ with viewing angle, and the spectra only change significantly blueward of $\sim 3500 \text{ \AA}$. In model DD2D_asym_01_dc3, however, the peak bolometric luminosity varies by $\sim 70\%$ with viewing angle, and the spectra are affected over a large fraction of the optical range (out to $\sim 6000 \text{ \AA}$).

These variations are not related to the total mass of ^{56}Ni synthesized during the explosion ($\sim 0.70 M_{\odot}$ and $\sim 0.64 M_{\odot}$ for DD2D_iso_06_dc2 and DD2D_asym_01_dc3, respectively); rather, they are a consequence of the *distribution* of ^{56}Ni in the ejecta. When the model is viewed from directions where ^{56}Ni extends to larger radii, the bolometric light curves peak earlier at a higher luminosity and are broader than for viewing angles where ^{56}Ni is confined to the deeper ejecta regions (see also Pinto & Eastman 2000a, their Fig. 4). The impact on the spectra is dramatic, owing to the higher ejecta temperatures (resulting in a bluer SED) and higher ionization (affecting the relative shapes and strengths of spectral features). For both models, the variation is largest at ultraviolet wavelengths, and is related to differences in the abundance of iron-group elements in the outer layers of the ejecta (see, e.g., Sauer et al. 2008).

The variation in peak bolometric luminosity with viewing angle in a given model (see Table 1) can thus be used to gauge the level of asymmetry in the ^{56}Ni distribution, but it does not constrain the level of isotropy in the distribution of ignition points. Most DD2D_iso models display variations in $L_{\text{bol,peak}}$ with viewing angle well below the 20% level, but others (DD2D_iso_04_dc3 and dc4) display factor-of-two variations. Likewise, some DD2D_asym models with the highest level of anisotropy in the distribution of ignition points (e.g. DD2D_asym_07_dc2 and dc3) display $\lesssim 10\%$ variations in peak bolometric luminosity with viewing angle, whereas the DD2D_asym_01 model series (which has an *isotropic* distribution of ignition points; see above) displays the largest variations (65–70%). This is not entirely surprising, since the ignition points are randomly distributed within a given setup, and individual ignition points that happen to be placed farther out than the bulk of the ignition sparks can easily dominate the flame morphology (this is especially true in 2D, which tends to favour large Rayleigh-Taylor structures; see Röpke et al. 2006).

2.2 Data

We largely rely on our database of light curves and spectra from the CfA Supernova Program to compare the models with observations. These include optical light curves of 251 SNe Ia (Riess et al. 1999b; Jha et al. 2006; Hicken et al. 2009), with near-infrared (NIR) photometry for the brighter objects (Wood-Vasey et al.

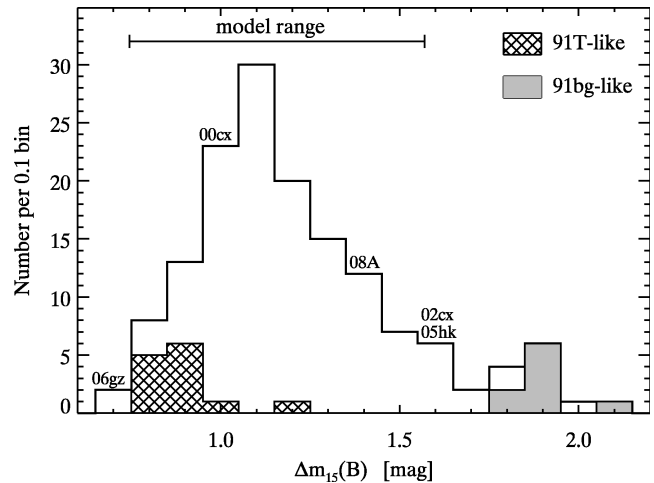


Figure 2. Distribution of the $\Delta m_{15}(B)$ decline rate parameter in our SN Ia sample with a maximum-light spectrum. SNe Ia with spectra resembling those of the luminous SN 1991T and the faint SN 1991bg are highlighted. Names of peculiar SNe Ia are given in their respective $\Delta m_{15}(B)$ bin. The horizontal error bar shows the $\Delta m_{15}(B)$ range in the 2D models of KRW09.

2008), and 2231 optical spectra obtained for the most part using the FAST spectrograph (Fabricant et al. 1998) mounted on the 1.5 m Tillinghast telescope at the Fred Lawrence Whipple Observatory (FLWO). The spectra have a typical FWHM resolution of 6–7 \AA with a rest-frame wavelength range 3500–7500 \AA . Already 577 SN Ia spectra have been published in several papers (the largest collection of 432 spectra of 32 SNe Ia has been published by Matheson et al. 2008) and are publicly available via the CfA Supernova Archive⁴. Additional spectra will be published in a forthcoming paper.

We complemented this data set with published data from the literature, and reference our sources where appropriate. Our study of rise times (§ 4.1) makes use of measurements on SN Ia light curves from the SDSS-II Supernova Survey by Hayden et al. (2010), as well as pseudo-bolometric light curves published by Stritzinger (2005).

The observed SN Ia sample used in this paper offers a fair representation of the true SN Ia population in the local Universe. Figure 2 shows the $\Delta m_{15}(B)$ distribution of SNe Ia for which we have a spectrum within three days from maximum light. This sample spans a large range in $\Delta m_{15}(B)$ ($\sim 0.7\text{--}2.1$ mag) and includes fractions of luminous 1991T-like ($\sim 9\%$), faint 1991bg-like ($\sim 7\%$), and peculiar 2002cx-like ($\sim 3\%$) SNe Ia comparable to those found by Li et al. (2011) for a volume-limited sample (9%, 15% and 5%, respectively). The fraction of 1991bg-like SNe Ia is a factor of two smaller than that reported by Li et al. (2011) and reflects a possible magnitude bias (the fraction drops from 15% to 3% for an ideal magnitude-limited sample; Li et al. 2011, their Fig. 11). In any case, the models of KRW09 do not extend beyond $\Delta m_{15}(B) \approx 1.6$ mag and none of their spectra present the prominent Ti II absorption band around 4000–4500 \AA characteristic of 1991bg-like SNe Ia. The fraction of 2002cx-like SNe Ia is also smaller than for the volume-limited sample of Li et al. (2011), but the reported rate has a large associated error.

³ We do note, however, that KRW09 present light curves for model DD2D_iso_06_dc2 until +60 d past B -and maximum in their Fig. 2.

⁴ <http://www.cfa.harvard.edu/supernova/SNarchive.html>

3 METHODS

In this section we present the general procedure for fitting model light-curves with empirical templates and for inferring intrinsic photometric properties from observed SN Ia light curves. We also present the algorithm used to cross-correlate the synthetic spectra with a large database of observed SN spectra, which we use as a basis for quantitatively evaluating each model.

3.1 Light-curve fits

We derive synthetic $UBVRI$ (Bessell 1990) and JHK_s (2MASS system; Cohen, Wheaton & Megeath 2003) magnitudes from the model spectra, with associated errors based on the number of photon packets in a given frequency bin. Typical errors at maximum light are < 0.005 mag in $UBVR$, < 0.01 mag in I , and progressively larger errors (0.015–0.05 mag) for JHK_s . We show the $UBVRIJHK_s$ light curves for model DD2D_iso_06_dc2 viewed along $\theta = 88^\circ$ in Fig. 3, compared to observations of SN 2003du (Anupama, Sahu & Jose 2005; Leonard et al. 2005; Stanishev et al. 2007) and the NIR template light curves of Mandel et al. (2009). The models appear to match the data well in the optical (albeit with significant differences in the U and I bands), but deviate in the near infrared.

3.1.1 Direct polynomial fits

We determine the time of maximum light and peak magnitude in the optical bands ($UBVR$), as well as the corresponding Δm_{15} decline rate. Our final estimates for the various quantities, along with their associated errors, are based on 1000 Monte Carlo realizations using the magnitude errors associated with each light-curve point. The resulting error on the fit parameters is below 0.1% in all cases.

3.1.2 Template-based fits

We attempt to fit $BVRI$ light curves for each model viewed from all 30 directions with three different light-curve “fitters” commonly used amongst SN observers: MLCS2k2 (Jha, Riess & Kirshner 2007), SALT2 (Guy et al. 2007), and SNooPy (Burns et al. 2011). To first order, these algorithms all share the common approach of comparing an input light curve with empirical templates based on observed data. Adding the U -band light curves for the MLCS2k2 and SALT2 fits (there are no standard U -band templates for SNooPy) has negligible impact on the results. Since no extinction is applied to the model synthetic magnitudes, we force the extinction to zero. This is not possible with SALT2, as the effects of extinction and intrinsic colour variations are described by a single parameter.

We show an example MLCS2k2 fit to the B -band light curve for model DD2D_iso_06_dc2 viewed along $\theta = 46^\circ$ in the left panel of Fig. 4 (*blue hatched area*). The fit is formally acceptable overall, with a reduced $\chi^2_\nu = 0.79$. However, a closer inspection shows that the MLCS2k2 template reaches its peak magnitude ~ 2.5 d earlier than the model predictions. This suggests that the models rise more slowly to maximum light than actually observed. In MLCS2k2 we have the possibility of fixing the time of maximum in the B band, and we use the value found from direct polynomial fits to the model light curves. The fits are severely degraded ($\chi^2_\nu = 3.37$; *orange hatched area*), and the empirical templates again appear to require a faster rise time than the models suggest.

This tension between model and empirical light-curve shapes

is not specific to MLCS2k2, as can be seen from the comparison with SALT2 and SNooPy on the B -band light curve for the same model/viewing angle combination (Fig. 4, *right panel*). In this particular example, the time of B -band maximum is underestimated by approximately 3 d, 2 d, and 1 d for MLCS2k2, SALT2, and SNooPy, respectively. The fits become formally worse following this same sequence, but this is due to the progressively smaller errors associated with the empirical templates (the mean absolute deviation of the template from the synthetic light curve over the time interval $-15 \leq t [\text{d}] \leq +20$ is ~ 0.7 mag for the three fitters).

A comparison of light-curve fits for all model/viewing angle combinations shows that, on average, MLCS2k2 underestimates $t_{\text{max}}(B)$ by ~ 2 d, SALT2 by ~ 0.5 d, and SNooPy by ~ 0.3 d. One might then be tempted to assume that the models have an overall shape that is compatible with the SNooPy empirical templates, but a comparison of $\Delta m_{15}(B)$ values inferred from these fits with those directly measured on the model light curves reveals a strong systematic trend (despite the residuals having a mean consistent with zero; see Fig. 5). The result is the same when we fix $t_{\text{max}}(B)$ to its actual value.

Given the difficulty for empirical templates to correctly reproduce the overall shape of the model light curves, in what follows we use the quantities derived from the direct polynomial fits (time of maximum, peak magnitude, post-maximum decline rate) for the models. The observed light curves are not always sufficiently well sampled to enable us to determine the time of maximum and $\Delta m_{15}(B)$ directly from polynomial fits, in which case we use values inferred from light-curve fitters. For SNe Ia for which we have both direct polynomial and template-based fits, the difference in time of maximum and decline rate from both methods is consistent with zero.

The various observables derived from the models are intrinsic to the supernova. Observations, however, are affected by extinction, both in the Milky Way and the SN host galaxy. The former is usually determined using the dust maps of Schlegel, Finkbeiner & Davis (1998), but the latter requires assumptions about the dust properties and the intrinsic colours of SNe Ia. In the next section we describe the BayeSN statistical model for SN Ia light curves (Mandel, Narayan & Kirshner 2011) used to infer the host-galaxy extinction and hence the intrinsic SN Ia peak magnitudes and colours.

3.1.3 Inferring intrinsic SN Ia properties with BayeSN

Mandel, Narayan & Kirshner (2011) constructed hierarchical Bayesian models for SN Ia light curves spanning optical through near infrared ($BVRIJH$) data. These statistical models describe the apparent distribution of light curves as a convolution of intrinsic SN Ia variations and a dust distribution. They modeled the intrinsic covariance structure of the full multi-band light curves, capturing population correlations between the intrinsic absolute magnitudes, intrinsic colours and light curve decline rates over multiple phases in the optical and NIR filters, as well as the distribution of host galaxy dust and an apparent correlation between the dust extinction A_V and its wavelength dependence, parameterized by R_V . The models use the optical and NIR time series data to fit individual SN Ia light curves, estimate their dust extinction and predict their distances. Probabilistic inference of the parameters of individual SNe Ia and also those describing the intrinsic SN Ia and dust populations are computed using a novel Markov Chain Monte Carlo code. These models were trained on a

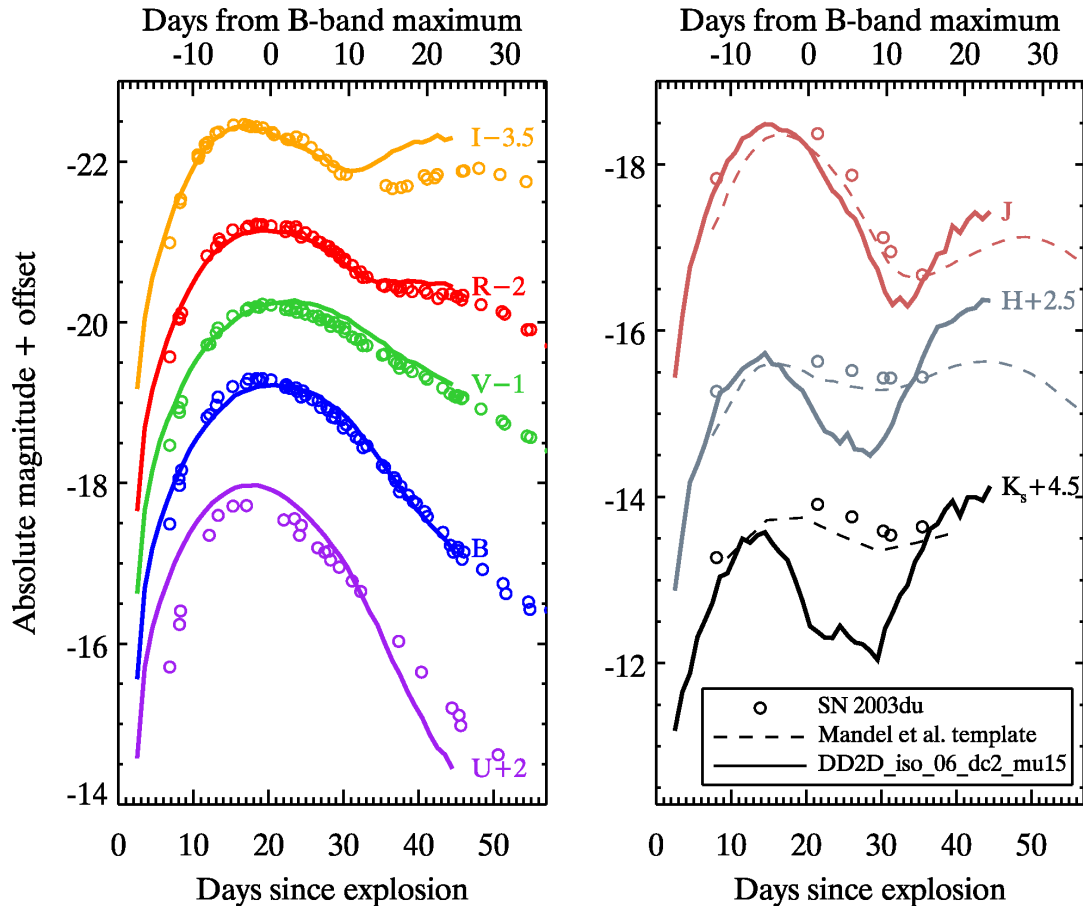


Figure 3. *UBVRIJHK_s* light curves for model DD2D_iso_06_dc2 viewed along $\theta = 88^\circ$ (solid lines). The open circles correspond to the light curves of SN 2003du (Anupama, Sahu & Jose 2005; Leonard et al. 2005; Stanishev et al. 2007), assuming a distance modulus $\mu = 32.79$ mag and no host-galaxy reddening (Stanishev et al. 2007). The dashed curves in the right panel are the NIR templates of Mandel et al. (2009), with updated templates for *J* and *H*.

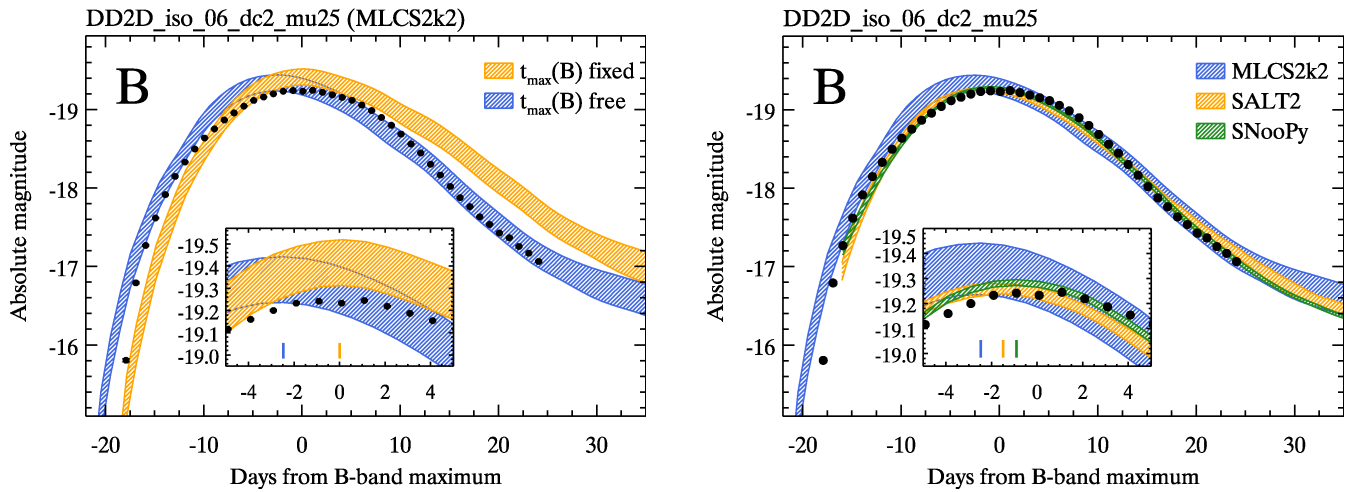


Figure 4. *Left:* Illustration of a light-curve fit using MLCS2k2 (Jha, Riess & Kirshner 2007) on the *B*-band light curve for model DD2D_iso_06_dc2 viewed along $\theta = 46^\circ$ (black dots). We show a fit fixing the time of *B*-band maximum ($t_{\max}(B)$) to its value measured from polynomial fits (orange), and a fit leaving $t_{\max}(B)$ as a free parameter (blue). The vertical tick marks denote the time of *B*-band maximum for the MLCS2k2 templates. Leaving $t_{\max}(B)$ free results in a formally better fit but the time of *B*-band maximum is underestimated (here by ~ 3 days). *Right:* comparison of light-curve fits to the same model using MLCS2k2 (blue), SALT2 (orange), and SNooPy (green). The vertical tick marks denote the time of *B*-band maximum for the template from the various fitters.

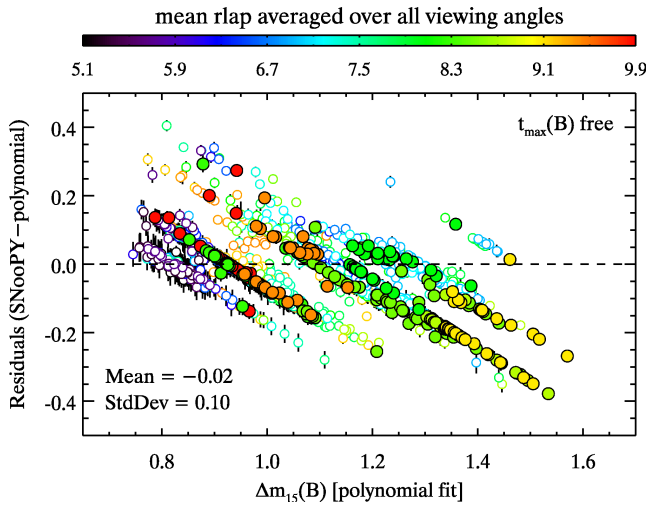


Figure 5. Difference between $\Delta m_{15}(B)$ inferred from SNooPy fits (where the time of B -band maximum is a free parameter) and that actually measured from polynomial fits. The colour-coding is used to distinguish individual models, where each model has 30 associated data points (one per viewing angle; see the discussion of Fig. 7 in § 3.3).

nearby ($z < 0.07$) set of SNe Ia with optical (CfA3, Hicken et al. 2009; Carnegie SN Program, Contreras et al. 2010) and NIR (PAIRITEL, Wood-Vasey et al. 2008) data, plus light curves from the literature with joint optical and NIR observations. The resulting Markov chain is used to estimate the dust extinction, apparent and absolute light curves, and intrinsic colours for each SN Ia. For this study, we employed the model that captures a linear correlation between R_V^{-1} and A_V , as this produced the best cross-validated distance predictions in Mandel, Narayan & Kirshner (2011).

3.2 Spectral comparison using SNID

We use the SuperNova IDentification (SNID) code of Blondin & Tonry (2007) to cross-correlate the synthetic spectra with a large database of observed spectra (referred to as “templates”). SNID is commonly used to determine the type, redshift, and age of a supernova spectrum (e.g. in IAU circulars). The database associated with the public release of SNID includes 493 spectra of 48 SNe Ia in the age range $-15 \leq t [\text{d}] \leq +30$. We have augmented it with new data from the CfA SN Program (see § 2.2) and recently published SN Ia data (SN 2005bl: Taubenberger et al. 2008; SN 2005cf: Garavini et al. 2007, Wang et al. 2009b; SN 2005cg: Quimby et al. 2006; SN 2005hj: Quimby, Höflich & Wheeler 2007; SN 2007ax: Kasliwal et al. 2008). This revised SNID database now includes 2046 spectra of 274 SNe Ia over the same age range. We refer the reader to Blondin & Tonry (2007) for an extensive discussion of the SNID algorithm. We point out here that both the input and template spectra are “flattened” through division by a *pseudo* continuum, such that the correlation relies on the *relative* shape and strength of spectral features, and is therefore insensitive to colour information, which can be intrinsic, or result from extinction by dust and flux-calibration uncertainties.

We first run SNID on the model spectra closest to B -band maximum light. We only consider SN Ia spectral templates, and force the redshift (usually a free parameter in SNID) to $z = 0$. We restrict the rest-frame wavelength interval over which the correlation is done to $3500\text{--}7500 \text{ \AA}$ to match the wavelength range of most

of the template spectra (see § 2.2). Last, we restrict the ages of the template spectra to be within 3 d from B -band maximum light (relaxing this age constraint does not significantly alter the results at maximum light). We are then left with 441 spectra of 175 SNe Ia in the SNID database.

The strength of a correlation between the input model spectrum and a particular template is embodied in the r_{lap} parameter, which is the product of the height of the normalized cross-correlation peak (the r -value of Tonry & Davis 1979) and the overlap in log-wavelength space between the input and template spectra (here $\text{lap} \approx \ln(7500/3500) \approx 0.7$). A correlation is considered good when $r_{\text{lap}} \geq 5$ (see Blondin & Tonry 2007). For each model/viewing angle combination, we record the best-match template (the one with the highest r_{lap}), as well as the mean r_{lap} value for the top five matches, which we consider a more reliable estimate of how similar a particular model spectrum is to observations. Fig. 6 shows some example SNID fits to our subset of eight models (see Table 1), viewed along the direction which provides the best match to an observed spectrum. The matches are good overall, with some discrepancies around 4000 \AA for some models.

We have also run SNID on model spectra at ages other than maximum light, namely $-10 \leq t [\text{d}] \leq +20$, each time imposing a ± 3 d age constraint on the template spectra. Close to maximum light ($-5 \leq t [\text{d}] \leq +5$), the fits are of similar quality as at maximum, i.e. the mean r_{lap} value for the cross-correlation with observed spectra is on average the same. However, further away from maximum light, the fits are degraded, and in some cases no good matches are found. Relaxing the age constraint for the template spectra results in formally better matches (higher mean r_{lap}), but the mean age of the top five matches tends to over- (under-) estimate the actual age for model spectra before (after) maximum light. This again suggests some differences between the rate at which the synthetic spectra evolve compared to observed spectra.

3.3 Model selection and the width-luminosity relation

Based on the SNID fits to the maximum-light model spectra, we can assign a “grade”, namely the mean r_{lap} value for the top five matches, to each model/viewing angle combination. Fig. 7 (*left*) shows the width-luminosity relation ($M_{\text{max}}(B)$ vs. $\Delta m_{15}(B)$) for the 2D delayed-detonation models of KRW09 (see their Fig. 3), where each point has now been colour-coded according to the mean r_{lap} value for that particular model/viewing angle. Points with higher r_{lap} values tend to lie systematically on the observed width-luminosity relation, i.e. the agreement between synthetic and observed spectra appears to translate into an agreement in photometric properties, thereby justifying our ranking scheme based on maximum-light spectra only (but see § 4.3).

Since each model has equal probability of being observed from one of the 30 different viewing angles (see § 2), it can only be validated if *all* viewing angles yield a good match to an observed SN Ia spectrum. Conversely, a lack of a good match for a *single* viewing angle should in principle lead us to reject the model as a whole, by which we mean it cannot be considered a valid approximation of observed SNe Ia. Six models fall in this category: DD2D_asym_03 (dc2 and dc3), DD2D_asym_06 (dc2 and dc3), and DD2D_asym_08 (dc2 and dc3). As their names suggest, all are models with an anisotropic distribution of ignition points. Moreover, they all have slow-declining light curves, with $0.76 \leq \Delta m_{15}(B) \leq 0.89$. While the DD2D_asym_03 models (dc2 and dc3) have 1-2 viewing angles with no good SNID matches, both

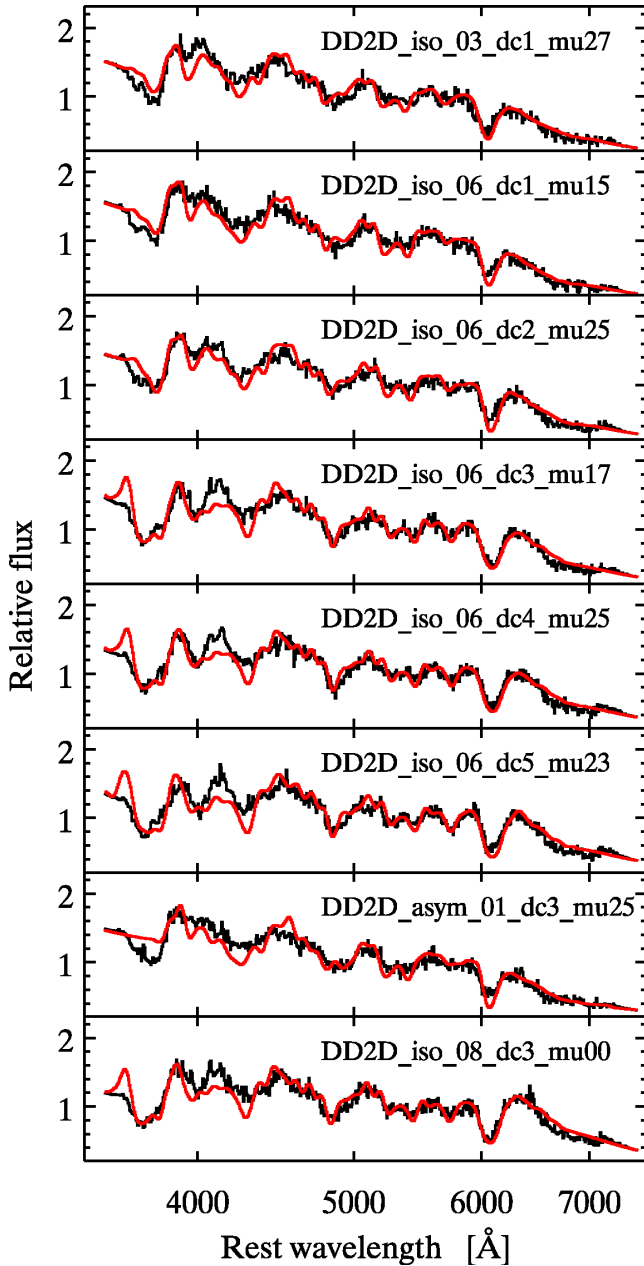


Figure 6. Results from SNID fits (red) to the B -band maximum-light spectra (black) for a subset of eight models, viewed along the direction which provides the best match to a spectrum in the SNID database.

DD2D_asym_06 and DD2D_asym_08 each have no good matches for more than half of the viewing angles.

We have selected a subset of eight models for detailed studies (Fig. 7, right): DD2D_iso_03_dc1 (red) is the model with the highest r_{lap} value overall; DD2D_asym_01_dc3 (orange) is the best model with a highly asymmetric distribution of ^{56}Ni ($\sim 70\%$ variation in peak bolometric luminosity; see Table 1); the complete DD2D_iso_06 model series (dc1 through dc5) has consistently high r_{lap} values and spans a large range of $\Delta m_{15}(B)$ (0.8–1.6 mag), thus enabling us to isolate the impact of the criterion for deflagration-to-detonation transition. It also includes the reference model DD2D_iso_06_dc2 used by KRW09 for detailed post-processing nucleosynthesis calculations. These seven models

all lie on the observed WLR and span a large range in synthesized ^{56}Ni mass (0.42–0.88 M_{\odot}). Last, DD2D_iso_08_dc3 (green; lower right) is the best model that does not lie on the width-luminosity relation. For all models other than DD2D_iso_03_dc1 and DD2D_iso_08_dc3, $\theta \approx 15^{\circ}$ corresponds to the direction of largest extent of ^{56}Ni distribution, and hence to the most luminous point in each model series. This is in part a consequence of the symmetry imposed on the explosion by the 2D axisymmetric setup in the models of KRW09. These models will be highlighted and their colour-coding preserved in subsequent figures.

In what follows we compare photometric (§ 4) and spectroscopic (§ 5) properties separately, as is commonly done in observational studies of SNe Ia. This in part reflects the way the observations are done (generally there are separate follow-up programmes for photometric and spectroscopic observations) and calibrated (individual photometric measurements have a typical absolute calibration accurate to a few percent, whereas individual spectra have a relative flux calibration that is generally less accurate; see, e.g., Matheson et al. 2008). In principle one would want to compare light curves and spectra simultaneously, and in fact we will refer to conclusions drawn in § 4 when discussing spectroscopic properties in § 5.

4 COMPARISON OF PHOTOMETRIC PROPERTIES

In this section we focus on multi-band light curves only, by comparing the rise times, maximum-light colours and colour evolution in models and data.

4.1 Rise times

As noted earlier (§ 3.1), the models rise too slowly to maximum light in the B band. We show the relation between the B -band rise time ($t_{\text{rise}}(B)$) and $\Delta m_{15}(B)$ in Fig. 8, for the 2D models of KRW09 (upper panel) and as measured on SN Ia light-curves from the SDSS-II Supernova Survey by Hayden et al. (2010) (where we exclude SNe Ia with $\Delta m_{15}(B) \gtrsim 1.6$ to match the $\Delta m_{15}(B)$ range of the models). In both cases $t_{\text{rise}}(B)$ appears to be largely independent of $\Delta m_{15}(B)$. The range of model rise times (18–23 d) overlaps with the observed distribution (13–23 d), although the bulk of the data display rise times smaller than 18 d. Within a given model, the rise time changes with viewing angle according to the distribution of ^{56}Ni along that particular inclination, anywhere between ~ 1 d and ~ 3 d. For model DD2D_iso_06_dc2, the B -band rise time is ~ 20 d regardless of viewing angle, while for model DD2D_asym_01_dc3, it varies between ~ 20 d ($\theta < 90^{\circ}$) and ~ 23 d ($\theta = 165^{\circ}$).

The model B -band rise times are more consistent with earlier measurements (e.g., 19.5 ± 0.2 d found by Riess et al. 1999a), but the latter were based on empirical templates that were “stretched” by equal amounts in the rising (pre-maximum) and falling (post-maximum) portions of the light curve. Strosvink (2007) considered asymmetric templates and found a mean rise time of 17.4 ± 0.4 d, subsequently confirmed by Hayden et al. (2010) using a larger data set.

The variation in rise times between various bands is linked to the redistribution of flux in frequency in the supernova ejecta. Fig. 9 shows the difference in time of maximum light with respect to the B band, for the $UVRIJ$ photometric bands as well as for the integrated $UBVRI$ (UVOIR) flux, where we have used polynomial fits to observed SN Ia $UBVRIJ$ light curves (again exclud-

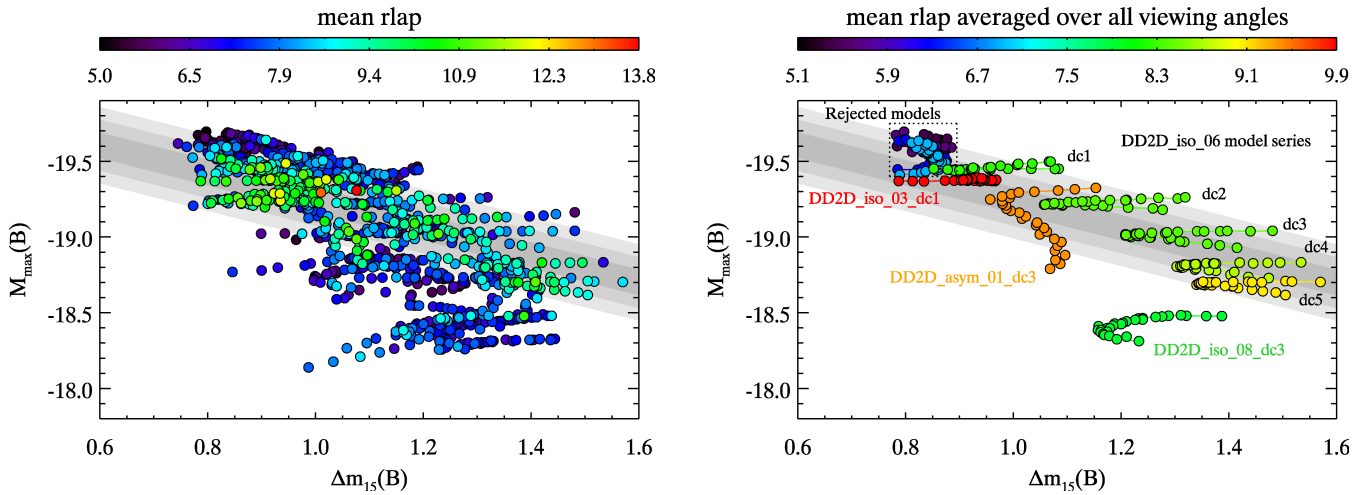


Figure 7. *Left:* peak absolute B -band magnitude vs. $\Delta m_{15}(B)$, for the 2D delayed-detonation models of KRW09. Each model has 30 associated data points, corresponding to a specific viewing angle. Each point is colour-coded according to the mean value of the SNID r_{lap} parameter for the best five matches to the maximum-light synthetic spectrum. The grey contours show the $1-3\sigma$ levels of the observed width-luminosity relation of Folatelli et al. (2010) with $\sigma = 0.1$ mag. *Right:* Same as left panel but for a subset of models. The colour-coding corresponds to the SNID r_{lap} parameter averaged over all viewing angles for any given model. For all models other than DD2D_iso_03_dc1 and DD2D_iso_08_dc3, $\theta \approx 15^\circ$ corresponds to the most luminous point in each model series. Models that lie in the dotted box are rejected based on the lack of any match to a maximum-light SN Ia spectrum in the SNID database for several viewing angles. These are: DD2D_asym_03 (dc2 and dc3), DD2D_asym_06 (dc2 and dc3), and DD2D_asym_08 (dc2 and dc3).

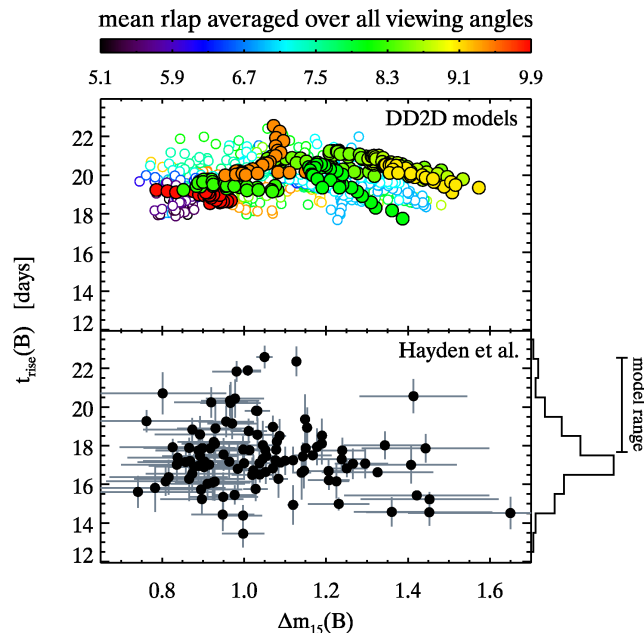


Figure 8. B -band rise time vs. $\Delta m_{15}(B)$, for the 2D delayed-detonation models of KRW09 (*top*) and for SN Ia data from Hayden et al. (2010) (*bottom*). The colour-coding is the same as in the right panel of Fig. 7 for the subset of selected models (*filled circles*). The open circles correspond to all other models. The rotated histogram in the lower panel shows the distribution of the Hayden et al. measurements, while the vertical error bar corresponds to the range of model rise times.

ing SNe Ia with $\Delta m_{15}(B) > 1.6$) from the literature for the data distributions (*open histograms*). The I -band and NIR light curves of SNe Ia display characteristic secondary maxima; here we report the time corresponding to the *first* maximum. The times of UVOIR maximum were derived from light curves published by Stritzinger (2005), where we used only SNe Ia with $UBVRI$ light curves so

as to minimize the uncertainty introduced by bolometric corrections which account for missing U -band data. These distributions are broadly consistent with those found on a more limited data set by Contardo, Leibundgut & Vacca (2000) (their Fig. 4).

The data indicate that SNe Ia peak in the U band typically ~ 2 d earlier than in B (consistent with Jha et al. (2006), who found $t_{\text{max}}(U) - t_{\text{max}}(B) = -2.3 \pm 0.4$ d), and $\sim 1-2$ d later in V and R . The I -band has a large spread in times of (first) maximum, but most SNe Ia peak ~ 2 d earlier than in B . The redder NIR bands peak even earlier (only J is shown in Fig. 9), as previously noted by several authors (e.g., Meikle & Hernandez 2000). Where a simplistic model would predict the reddest bands to peak the latest as the temperature of the ejecta decreases (and this explains the $t_{\text{max}}(U) < t_{\text{max}}(B) < t_{\text{max}}(V)$ sequence), the fact that the IJK_s bands peak before the B band shows that flux is efficiently redistributed from the ultraviolet to the near infrared (e.g., Pinto & Eastman 2000b). The magnitude of this effect is strongly dependent on the ionization stage of iron-group elements in the SN Ia core, and is responsible for the secondary maxima observed in IJK_s SN Ia light curves (see Kasen 2006).

This trend is broadly reproduced by the models, with a large overlap with the observations in $VRIJ$, and a more marginal overlap in U (especially when considering our subset of selected models). The distribution of the difference between UVOIR and B -band maxima in the models, however, has no overlap with the observed distribution. The data seem to indicate that the times of UVOIR and B -band maxima coincide (see also Contardo, Leibundgut & Vacca 2000), whereas the model bolometric light curves peak $1-2$ d earlier than the B -band. The U band contributes most to this (modest) discrepancy, as it is the brightest band at maximum light in these models.

4.2 Maximum-light colours

Fig. 10 shows the normalized distributions of intrinsic $U - B$, $B - V$, $B - R$, $V - R$, $V - I$, and $V - J$ colours at B -band maxi-

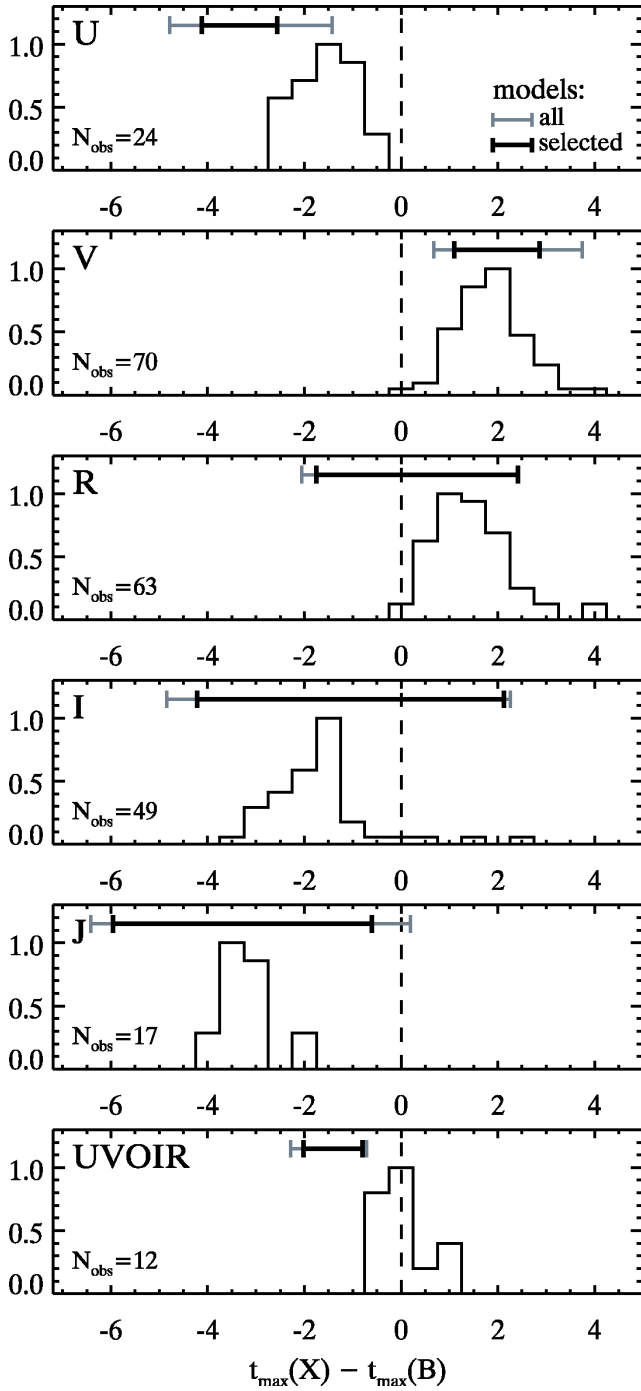


Figure 9. Difference between the time of maximum light in *UVRIJ* (and in *UVOIR* flux) and the time of *B*-band maximum as observed in actual data (*open histograms*), and ranges of the same quantity for all models (*gray error bars*) and our subset of selected models (*black error bars*).

mum as inferred from BayeSN fits to actual data (*open histograms*) compared with the ranges for the 2D models of KRW09 (*gray*: all models; *black*: subset of selected models). The data indicate that SNe Ia have an intrinsic $B - V \approx -0.1$ mag at *B*-band maximum, whereas the models have a systematically redder $B - V$ colour (0.0–0.2 mag). This was already noted by KRW09 and attributed to the approximate treatment of non-LTE effects. The distributions for $B - R$, $V - R$, and $V - I$ have a large overlap between the

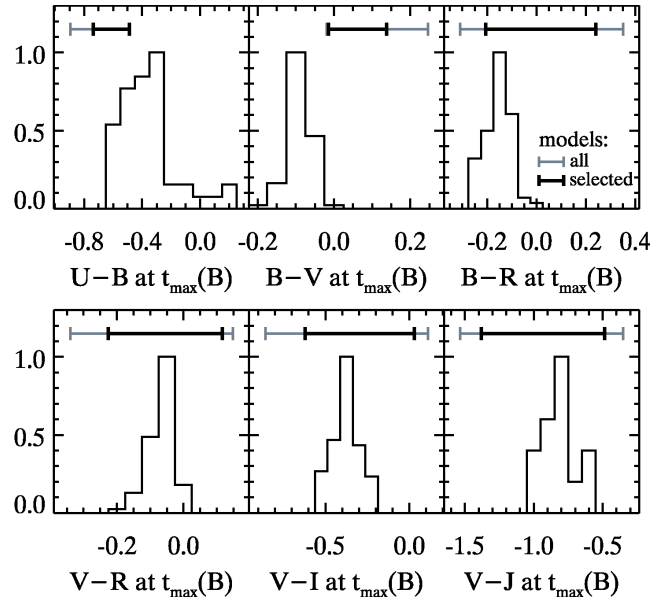


Figure 10. Comparison of intrinsic rest-frame colours at *B*-band maximum as inferred from BayeSN fits to actual data (*open histograms*) with those for all models (*gray error bars*) and our subset of selected models (*black error bars*). The $U - B$ colour distribution is derived from MLCS2k2 fits to SNe Ia with low visual extinction ($A_V < 0.1$ mag).

models and data, but contrary to the $B - V$ colour the former have a much larger spread (this is also true when only considering the subset of selected models). The $V - J$ colour displays differences of up to ~ 0.5 mag between the models and the data, albeit with a large overlap with the observed distribution.

The models have a systematically redder $B - V$ colour at *B*-band maximum, but they are systematically *bluer* in $U - B$ colour (Fig. 10). Mandel, Narayan & Kirshner (2011) did not include *U*-band data in their analysis to avoid calibration uncertainties, so we instead infer the intrinsic *U*-band magnitude based on MLCS2k2 fits to SNe Ia with low visual extinction ($A_V < 0.1$ mag). The models show some overlap in $U - B$ colour with the data, but extend $\gtrsim 0.2$ mag further in the blue. This excess of *U*-band flux can be explained either by a hotter ejecta temperature affecting the overall SED or an incomplete description of line-blanketing of UV photons and subsequent redistribution of flux to redder wavelengths, or a combination of both. Since the impact of such effects is most easily seen on the spectra, we will discuss them in § 5.

More luminous SNe Ia are also intrinsically bluer (this is known as the “brighter-bluer” relation, e.g. Tripp 1998). Its degeneracy with extinction by dust (SNe Ia obscured by dust will appear redder) is exploited by some light-curve fitters to describe the effects of extinction and intrinsic colour variations using a single parameter (e.g., SALT2: Guy et al. 2007). The brighter-bluer relation (i.e. $M_{\max}(B)$ vs. intrinsic $B - V$ at *B*-band maximum) derived from BayeSN fits to actual data is shown in the upper-left panel of Fig. 11 (*dashed line*). The 2D models of KRW09 also follow a brighter-bluer relation, but it is significantly steeper than observed. This difference is not surprising given the lack of overlap in $B - V$ colour between the models and the data (Fig. 10).

The agreement between models and data is significantly better when considering $M_{\max}(B)$ vs. $B - R$ at *B*-band maximum (Fig. 11, *upper-right panel*), which forms an extremely tight relation. Small deviations are apparent for $B - R \gtrsim 0$ mag, where the models predict peak colours that are much redder than inferred

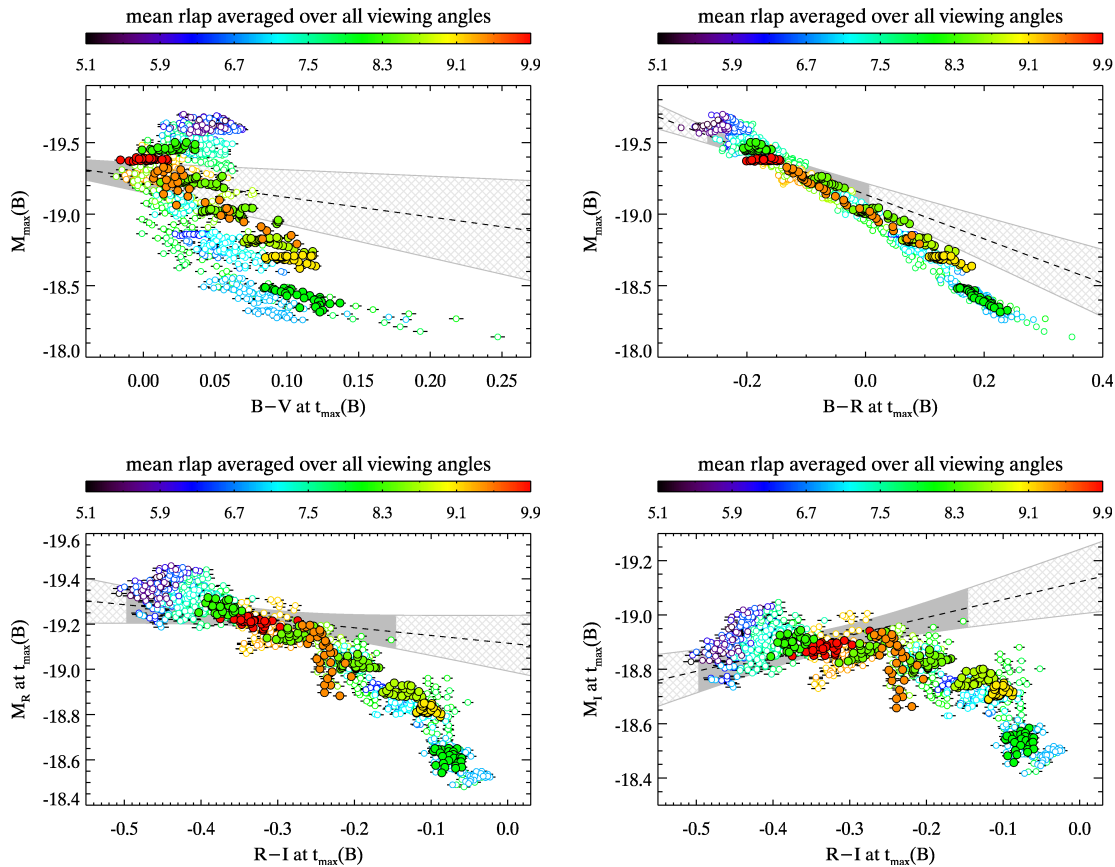


Figure 11. Intrinsic magnitudes vs. intrinsic colours at B -band maximum. The colour-coding is the same as in Fig. 9. The grey contour corresponds to the 95% confidence level of the observed relation inferred from BayeSN fits to actual data (*dashed line*). The grey shaded area highlights the colour range in the data used to determine the observed relation, while the grey hatched area corresponds to extrapolations of this relation.

from observations (Fig. 10). Of all the selected models, model DD2D_asym_01_dc3 (*filled orange circles*) displays the largest variation of $B - R$ colour (the same is true to a lesser extent when considering the $B - V$ colour), illustrating the greater change of the overall SED with viewing angle stemming from the asymmetric ^{56}Ni distribution (see Fig. 1).

The lower panels of Fig. 11 show M_R and M_I vs. intrinsic $R - I$ colour (all quantities are at B -band maximum). While M_R has almost no relation to $R - I$ colour (the slope is consistent with zero at $\sim 1\sigma$), M_I vs. $R - I$ appears to define a brighter-redder relation⁵. In both cases, models that predict redder $R - I$ colours than inferred from observations lie off the relation.

4.3 Colour evolution

The early-time evolution of SN Ia colours results from a complex interplay between a gradual cooling of the ejecta and changes in ionization stages of several species, leading to order-of-magnitude changes in the opacity at selected frequencies. In particular, the III \rightarrow II recombination of iron-group elements is responsible for most of the redistribution of flux from blue to red wavelengths and its timescale controls the rate of colour evolution in SNe Ia (see Kasen & Woosley 2007).

⁵ While this is not the subject of this paper, such a relation would help break the degeneracy between extinction by dust and intrinsic colour variations.

Fig. 12 shows the time evolution of $U - B$, $B - V$, $B - R$, $V - R$, $V - I$ and $V - J$ colours for our subset of selected models (we have chosen one representative model for the DD2D_iso_06 series, namely DD2D_iso_06_dc2), colour-coded according to the viewing angle θ . Overplotted are observed (dereddened) colour curves from SNe Ia in similar $\Delta m_{15}(B)$ ranges, except for the $V - J$ colour curves where we show the Krisciunas et al. (2004) templates for slow- ($0.8 \lesssim \Delta m_{15}(B) \lesssim 1.0$) and mid-range ($1.0 \lesssim \Delta m_{15}(B) \lesssim 1.4$) decliners, as well as for SN 2001el ($\Delta m_{15}(B) \approx 1.1$). To minimize the uncertainties associated with extinction corrections, we only include SNe Ia with a visual extinction $A_V < 0.25$ mag, as inferred from BayeSN fits.

The $B - V$ colour evolution of the models is largely consistent with that seen in the data, with small systematic offsets to redder colours for model DD2D_iso_08_dc3, which lies off the width-luminosity relation. The agreement between the models and the data for the $B - R$ colour evolution is also satisfactory, apart for model DD2D_iso_03_dc1, whose $B - R$ colour becomes progressively bluer with age until ~ 10 d past B -band maximum while the data become redder over the same time interval. The disagreement is exacerbated when considering $V - R$ for this model, but the $V - I$ colour evolution is in good agreement (as is true for the other models of Fig. 12). Interestingly, DD2D_iso_03_dc1 is our best overall model based on cross-correlations with observed spectra using SNID (see § 3.3). Since SNID compares the *relative* shapes and strengths of spectral features, the overall SED was not taken into account when ranking these models, which allows

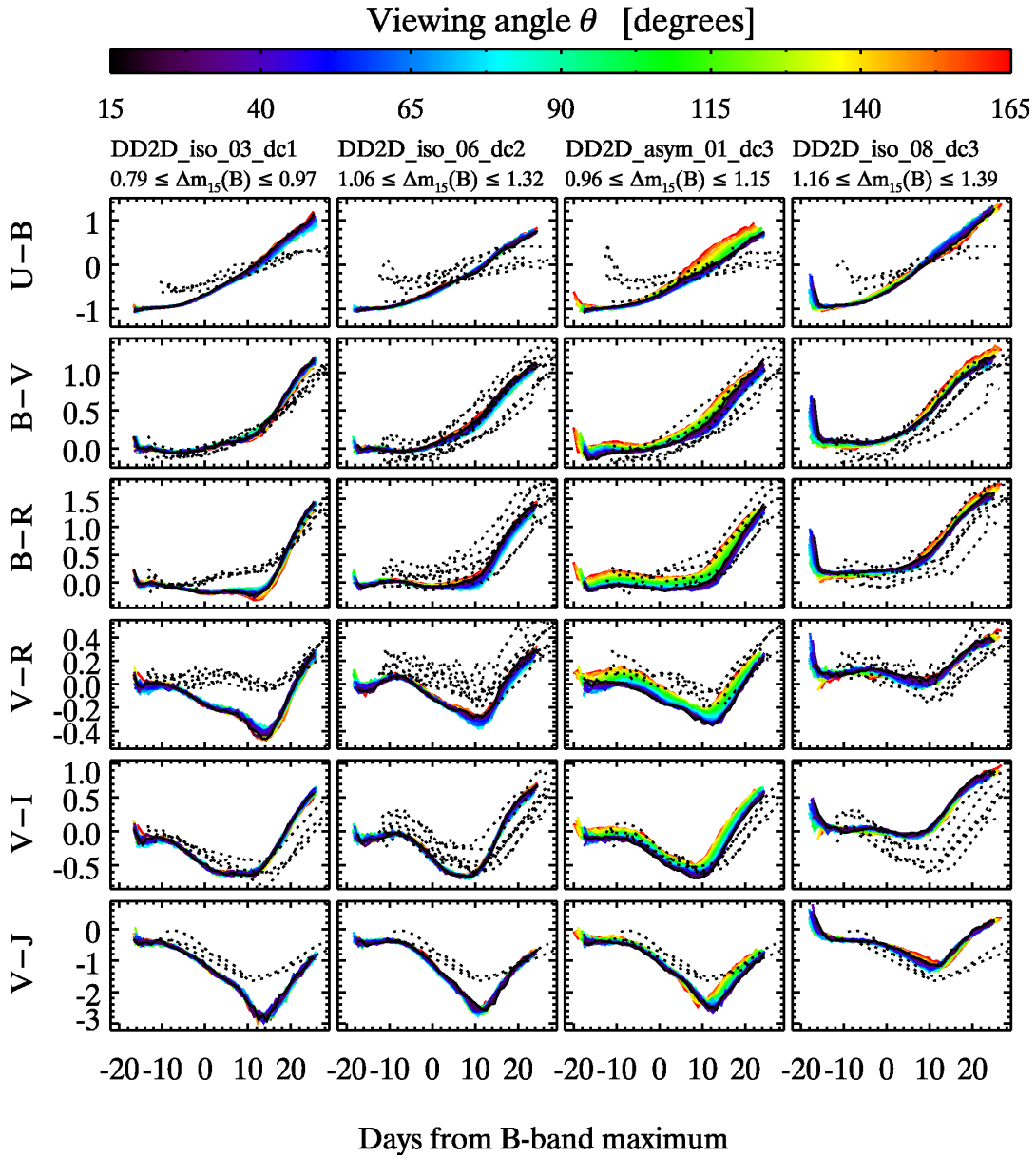


Figure 12. Time evolution of intrinsic colours measured at B -band maximum for four of our selected models, colour-coded according to the viewing angle θ . The dotted lines for $U - B$, $B - V$, $B - R$, $V - R$, and $V - I$ correspond to dereddened colour curves from observed SNe Ia with low visual extinction ($A_V < 0.25$ mag as inferred from BayeSN fits) in similar $\Delta m_{15}(B)$ ranges. The dotted lines for $V - J$ correspond to templates for slow ($0.8 \lesssim \Delta m_{15}(B) \lesssim 1.0$) and mid-range ($1.0 \lesssim \Delta m_{15}(B) \lesssim 1.4$) decliners, as well as for SN 2001el ($\Delta m_{15}(B) \approx 1.1$), from Krisciunas et al. (2004).

for possibly large offsets in broadband colours between our selected models and the data. Based on the $V - R$ colour evolution, one would rank model DD2D_iso_08_dc3 highest of the four models shown in Fig. 12, where in fact it is the only model that does *not* lie on the observed width-luminosity relation. As noted earlier, model DD2D_asym_01_dc3 displays the largest colour variation at any given time.

The colour curves for $U - B$ and $V - J$, however, reveal the largest inconsistencies between the models and the data. All the models have a systematically bluer $U - B$ colour at early times (up until ~ 10 d past B -band maximum), and increasingly redder $U - B$ colours at later times. By 20 d past B -band maximum, the models display a $U - B$ colour that is ~ 0.5 mag too red with

respect to the data, a difference that clearly cannot be explained by simple U -band calibration uncertainties.

The qualitative behaviour of the $V - J$ colour curves is compatible with the data, but displays large offsets ($\gtrsim 1$ mag for model DD2D_iso_03_dc1) around ~ 10 d past B -band maximum, which corresponds to the time of flux minimum between the two J -band maxima (see Fig. 3). This is not the case for model DD2D_iso_08_dc3, which has *redder* $V - J$ colours at any given time when compared to observations. The failure of the models to properly reproduce the NIR flux in SNe Ia at all times could be due in part to the atomic data used in the radiative transfer calculations, as noted by Kasen (2006). By comparing J -band light curves computed with the 500,000 line Kurucz CD 23 and the 42 million line Kurucz CD 1, he showed that including more lines re-

sulted in ~ 1 mag more J -band flux between -10 and $+20$ days from B -band maximum and a shallower flux minimum (his Fig. 5), although it is not clear which lines contribute most to this effect. Other approximations used in the radiative transfer calculations (LTE, expansion opacity formalism, equivalent two-level atom for flux redistribution etc.) could also explain part of these discrepancies.

Fig. 12 conveys the message that a direct comparison of SN Ia models with observations must involve both photometric and spectroscopic properties. Our highest-ranked model based on cross-correlations with spectral templates using SNID is DD2D_iso_03_dc1, yet its colour curves present the largest level of disagreement with observations. We also note that DD2D_iso_08_dc3 fares best based on the evolution of its broadband colours, yet it lies off the observed width-luminosity relation.

5 COMPARISON OF SPECTROSCOPIC PROPERTIES

It is difficult to resolve discrepancies between the models and data based on photometric measurements alone, and we now turn to the comparison of spectroscopic properties, first considering spectra at maximum light (§ 5.1), and then their evolution with time (§ 5.2).

5.1 Maximum-light spectra

5.1.1 Spectroscopic diversity at a given $\Delta m_{15}(B)$

We would like to compare the general appearance of the model spectra in specific $\Delta m_{15}(B)$ ranges. To do this we select two narrow $\Delta m_{15}(B)$ ranges (± 0.05 around a central value) that include at least one viewing angle for each of the eight models in our subset. Based on Fig. 7, we see that three of our subset of selected models overlap at $\Delta m_{15}(B) \approx 0.95$ (DD2D_iso_03_dc1, DD2D_iso_06_dc1, and DD2D_asym_01_dc3), while the remaining five overlap at $\Delta m_{15}(B) \approx 1.3$ (DD2D_iso_06_dc2 through dc5 and DD2D_iso_08_dc3). We thus define our $\Delta m_{15}(B)$ ranges of interest as 0.90–1.00 and 1.25–1.35. Figure 13 shows observed maximum-light spectra in both $\Delta m_{15}(B)$ ranges (*black*) compared to our subset of selected models (*red*), for which we only show spectra for one viewing angle (the one that yields a $\Delta m_{15}(B)$ closest to the middle of the $\Delta m_{15}(B)$ range considered). The observed spectra all have an estimated visual extinction $A_V < 0.25$ mag and have been dereddened.

For $0.90 \leq \Delta m_{15}(B) \leq 1.00$, the observed sample consists of both “normal” and 1991T-like SNe Ia (of which SN 1998es, SN 1999aa, SN 1999dq; all from Matheson et al. 2008). The latter are characterized by hot ejecta, with evidence for lines of doubly-ionized iron-group elements (Fe III/Co III) in place of lines of Fe II/Co II in maximum-light spectra of “normal” SNe Ia, and which explains part of the observed variation around ~ 4300 Å. Redward of this, the spectra are remarkably similar to one another, albeit with variations in the strength of the absorption component of the prominent Si II $\lambda 6355$ line (1991T-like SNe Ia have shallower Si II absorptions). The model spectra in the same $\Delta m_{15}(B)$ range are also similar to one another, but they have a much bluer (hotter) SED than the data (as noted based on the comparison of $U - B$ colours in § 4.2), and shallower Si II $\lambda 6355$ absorptions. This line is also broader and its absorption component more blueshifted than observed in the data, both evidence for larger ejecta velocities. Several small-scale features present in the data are thus “washed out” in the models, as the higher expansion velocities increase the line

overlap. This is clearly seen in the S II $\lambda 5454,5640$ doublet, which appears as two distinct absorption components in all the observations but which is barely resolved in the models (and not resolved at all for model DD2D_iso_03_dc1).

For $1.25 \leq \Delta m_{15}(B) \leq 1.35$, the observed sample consists almost exclusively of “normal” SNe Ia, apart from SN 2004dt which displays larger absorption velocities (clearly visible in the Si II $\lambda 6355$ line) and was found by Wang et al. (2006) to have the highest degree of polarization ever measured in a SN Ia. SN 2004eo was labeled “transitional” by Pastorello et al. (2007) due to its intermediate properties between normal and underluminous SNe Ia. The model spectra in the same $\Delta m_{15}(B)$ range show a large degree of heterogeneity, both in the slope of the overall SED and in the relative shapes and strengths of spectral features. Model DD2D_iso_06_dc2 is too blue compared to observations, and displays relatively shallow absorption features; conversely, models DD2D_iso_06_dc4 and dc5 have a significantly redder SED with broader and deeper absorption features than in the observations, as clearly seen from the three prominent Si II absorption features at ~ 4000 Å, ~ 5800 Å, and ~ 6100 Å. Model DD2D_iso_08_dc3 fares better both in terms of SED slope and relative strengths of spectral features, albeit with less prominent absorption around ~ 4300 Å and lack of small-scale structure around ~ 4800 Å (both features are predominantly due to lines of Fe II/Co II, with important contributions from Mg II and Ti II). As was the case for the model spectra with smaller $\Delta m_{15}(B)$ (Fig. 13, *left panel*), the S II $\lambda 5454,5640$ doublet is not resolved in this model (the same is also true for DD2D_iso_06_dc2).

The partial failure of the models to reproduce the relative shapes and strength of the Si II lines impacts their ability to reproduce the observed correlation of several spectroscopic indicators with $\Delta m_{15}(B)$ (see, e.g., Blondin, Mandel & Kirshner 2011). Fig. 14 shows two such indicators, namely the $\mathcal{R}(\text{Si})$ ratio of Nugent et al. (1995) (defined as the ratio of the relative absorption depth of the Si II $\lambda 5972$ line to that of Si II $\lambda 6355$) and the *pseudo* equivalent width (pEW) of Si II $\lambda 4130$ (see Arsenijevic et al. 2008; Walker et al. 2010; Blondin, Mandel & Kirshner 2011; Chotard et al. 2011). There is a clear correlation between both indicators and $\Delta m_{15}(B)$ in our spectroscopic data set (*lower panels*), albeit with two significant outliers for $\mathcal{R}(\text{Si})$ (one of which SN 2006bt, whose peculiar nature has been discussed at length by Foley et al. 2010). A linear fit to the data is shown in both cases (*dashed line*) and overplotted on measurements from the models (*upper panels*). There is no clear correlation between $\mathcal{R}(\text{Si})$ and $\Delta m_{15}(B)$ in the models, but the measurements have a large associated error due to Monte Carlo noise affecting the weaker Si II $\lambda 5972$ line. As for Si II $\lambda 4130$, there is a general trend of increasing pEW with $\Delta m_{15}(B)$, but with a large scatter for $\Delta m_{15}(B) \gtrsim 1.1$ caused by some model spectra with unusually broad and deep absorptions.

5.1.2 Composite spectra at a given $\Delta m_{15}(B)$

To better study overall systematic differences between the models and observations, we generate composite spectra using the same pre-processing as done by SNID: the individual spectra are “flattened” through division by a *pseudo* continuum. We then compute the mean flux in each wavelength bin, as well as the standard deviation from the mean. The result is a composite spectrum with error bands, which we show in Fig. 15. Note that the composite spectra based on observations (*hatched grey*) only uses the sample of spectra shown in Fig. 13, while those based on the models comprise all

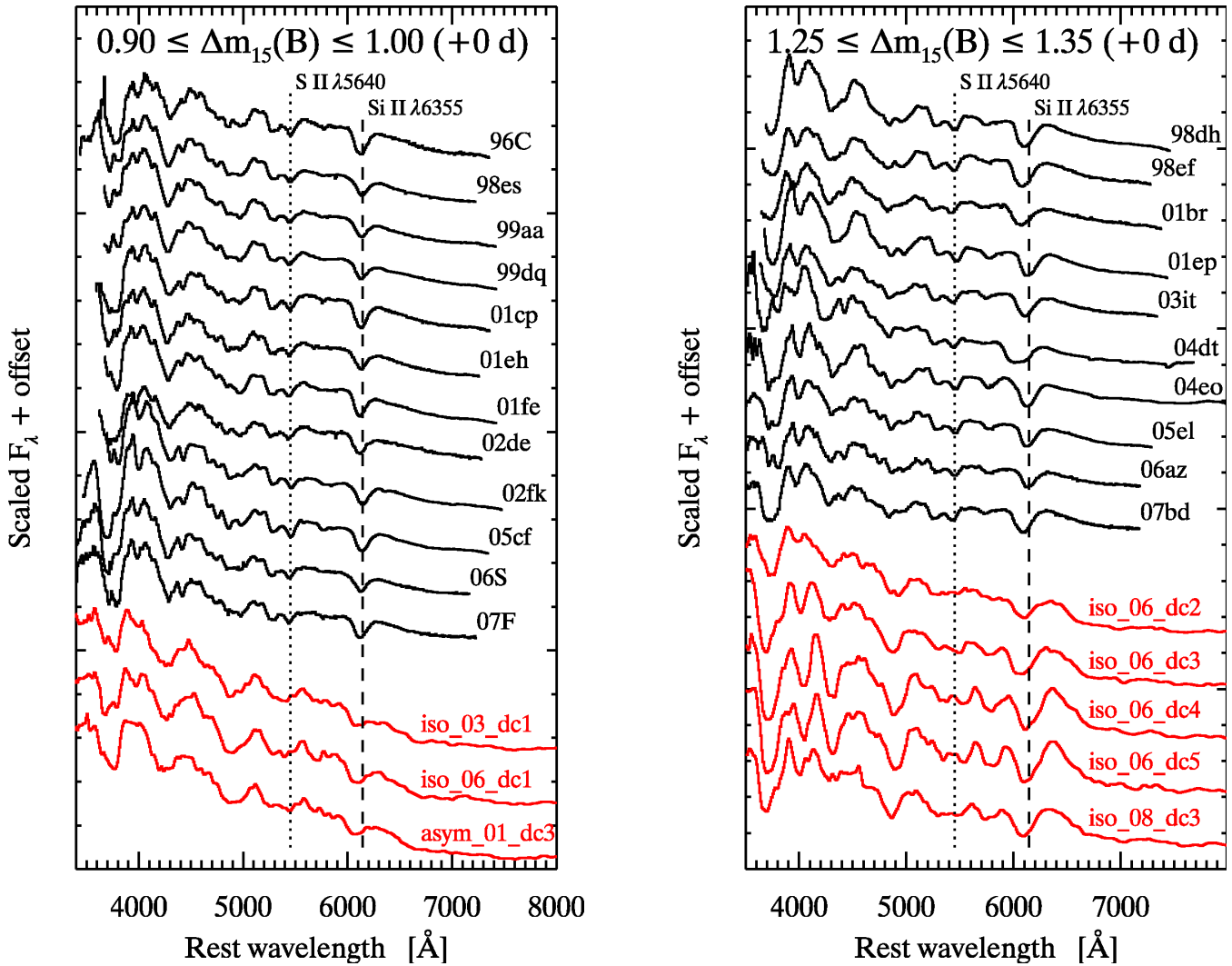


Figure 13. Maximum-light spectra for $0.90 \leq \Delta m_{15}(B) \leq 1.00$ (left) and $1.25 \leq \Delta m_{15}(B) \leq 1.35$ (right) compared to models in the same $\Delta m_{15}(B)$ range. For sake of clarity, we only show spectra corresponding to our subset of selected models, and select the viewing angle corresponding to the decline rate closest to the middle of the $\Delta m_{15}(B)$ range considered. The vertical lines correspond to S II $\lambda 5640$ (dotted) and Si II $\lambda 6355$ (dashed) blueshifted by 10000 km s^{-1} .

viewing angles which yield a $\Delta m_{15}(B)$ in the appropriate range. The composite spectra for all (selected) models thus consists of 234 (50) and 150 (41) individual spectra for $0.90 \leq \Delta m_{15}(B) \leq 1.00$ and $1.25 \leq \Delta m_{15}(B) \leq 1.35$, respectively.

The composite spectra for $0.90 \leq \Delta m_{15}(B) \leq 1.00$ confirm the shallower absorptions and larger blueshifts of spectral lines in the models. The location of maximum absorption in the Si II $\lambda 6355$ line is typically $\sim 100 \text{ \AA}$ too blue in the models, corresponding to a $\sim 5000 \text{ km s}^{-1}$ difference in absorption velocity. The small-scale structure in the two iron-group-dominated absorption features ($\sim 4300 \text{ \AA}$ and $\sim 4800 \text{ \AA}$) present in the data is not seen in the models, as mentioned earlier. The emission component of the Si II $\lambda 6355$ line appears to be relatively stronger in the models, but this is an artefact of the division by a pseudo continuum. The flux level in the models drops significantly redward of $\sim 6500 \text{ \AA}$ compared to the data, artificially enhancing the relative strength of the Si II $\lambda 6355$ emission profile after division by this pseudo continuum.

The composite spectra for $1.25 \leq \Delta m_{15}(B) \leq 1.35$ do not seem to support the apparent heterogeneity of the model spectra in Fig. 13. This is not surprising since Fig. 13 only shows 5 of the

150 (41) spectra used to generate the composite spectrum for all (selected) models. It is also possible that the division by a pseudo continuum attenuates some of these differences. Nonetheless, the composite spectra for this $\Delta m_{15}(B)$ range do reveal some interesting properties of the models. The absorption velocity offset is less pronounced in the Si II lines. The location of maximum absorption in the Si II $\lambda 4130$ line even appears to be at larger wavelengths in the models, but this could result from line overlap. The two iron-group-dominated features at $\sim 4300 \text{ \AA}$ and $\sim 4800 \text{ \AA}$ again appear to be smoothed by a larger expansion velocity field. The S II doublet is again shallower in the models, although better resolved than for $0.90 \leq \Delta m_{15}(B) \leq 1.00$. Both absorption components appear to be slightly offset to redder wavelengths when compared to the data, although the difference is typically $\lesssim 25 \text{ \AA}$, or $\lesssim 1500 \text{ km s}^{-1}$. The emission component of the Si II $\lambda 6355$ line is again artificially enhanced via the division by a pseudo continuum, although part of the difference is real and clearly seen in the model spectra shown in Fig. 13 (in particular for models DD2D_iso.06.dc4 and dc5). We will explore some of these systematic differences in more detail by focusing on this line in the next section.

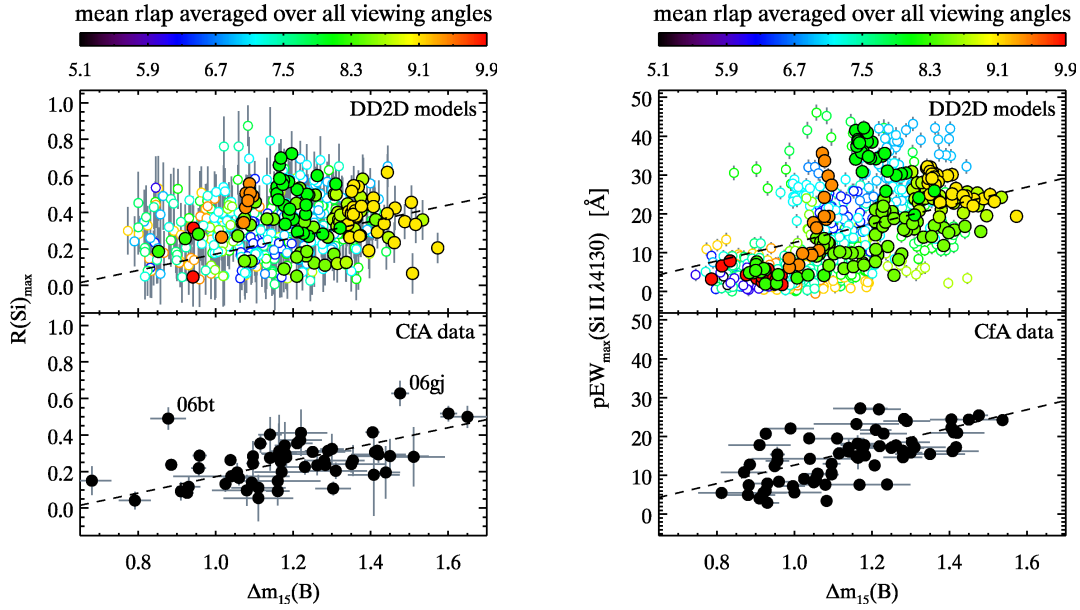


Figure 14. *Left:* Spectroscopic indicator $\mathcal{R}(\text{Si})$ vs. $\Delta m_{15}(B)$, for the 2D delayed-detonation models of KRW09 (*top*) and for SN Ia data from the CfA SN Program (*bottom*). The colour-coding is the same as in the right panel of Fig. 7. The dashed line is a linear fit to the CfA data, and is overplotted in the upper panel. The points corresponding to the outliers SN 2006bt and SN 2006gj are labeled accordingly. *Right:* pseudo-EW of the Si II 4130 line vs. $\Delta m_{15}(B)$.

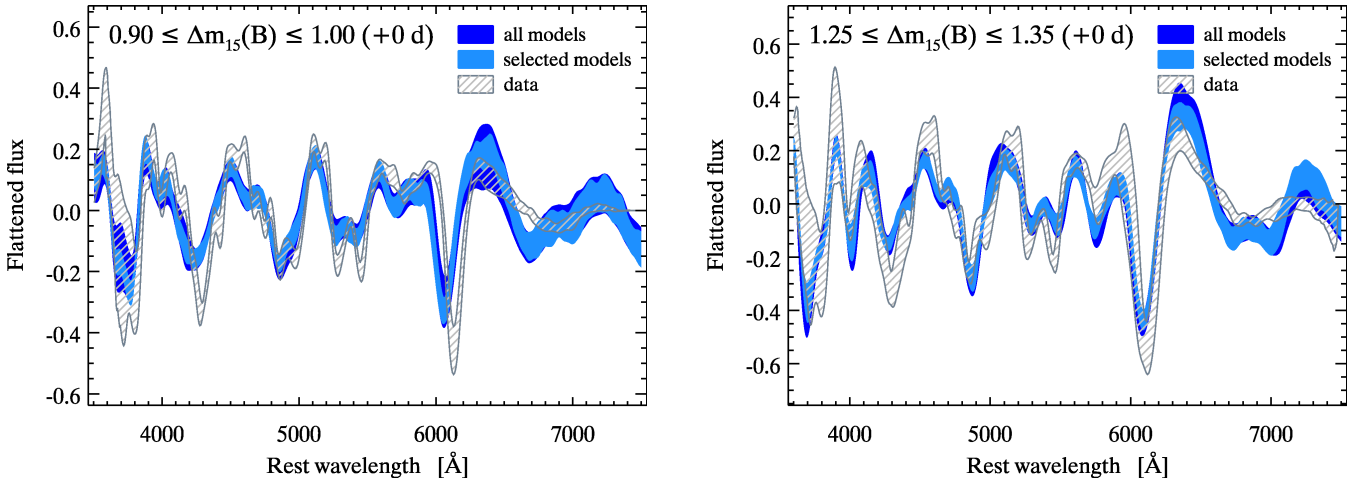


Figure 15. Composite maximum-light spectra for $0.90 \leq \Delta m_{15}(B) \leq 1.00$ (*left*) and $1.25 \leq \Delta m_{15}(B) \leq 1.35$ (*right*). The shaded bands correspond to the standard deviation about the mean maximum-light spectrum. We show the flattened composite spectra for all DD2D models (*filled dark blue*), our subset of selected models (*filled light blue*) and as observed based on the sample of spectra shown in Fig. 13 (*hatched grey*).

5.1.3 Si II 6355 absorption velocity

Wang et al. (2009a) introduced a classification scheme for SNe Ia based on the Si II 6355 absorption velocity at maximum light. By considering deviations from an empirical mean trend, they classified their SN Ia sample into “normal” and “high-velocity” subclasses, with separate subclasses for 1991T- and 1991bg-like SNe Ia. Fig. 16 (*lower panel*) shows the relation between the pseudo equivalent width of the Si II 6355 line with its absorption velocity (i.e. the velocity at maximum absorption, v_{abs}) within 3 d from maximum light in our spectroscopic sample from the CfA SN Program (see Wang et al. 2009a, their Fig. 2). Only SNe Ia with $\Delta m_{15}(B) \lesssim 1.6$ are included, to match the $\Delta m_{15}(B)$ range of the models. We added a random component drawn from a 500 km s^{-1} -wide uniform distribution to account for velocity measurement er-

rors resulting from the 10 \AA binning in the synthetic spectra. We have also run one model (DD2D_iso_06_dc2) with a larger number of photon packets (10^9 instead of 10^8) and find the measurements to be consistent with the lower-S/N model run. Almost all the models have Si II 6355 absorption velocities consistent with the “high-velocity” subclass, regardless of the viewing angle, in agreement with the large blueshifts discussed in the previous section. Several models have significantly lower pEW than in the data (at a given v_{abs}), again consistent with the shallower absorptions seen in some of the individual spectra (in particular, those in the $0.90 \leq \Delta m_{15}(B) \leq 1.00$ range).

These measurements reveal further properties of the models themselves. Model DD2D_asym_01_dc3 (*filled orange circles*) displays the largest variation in Si II 6355 absorption velocity ($-11000 \gtrsim v_{\text{abs}} \gtrsim -15000 \text{ km s}^{-1}$), the larger blueshifts cor-

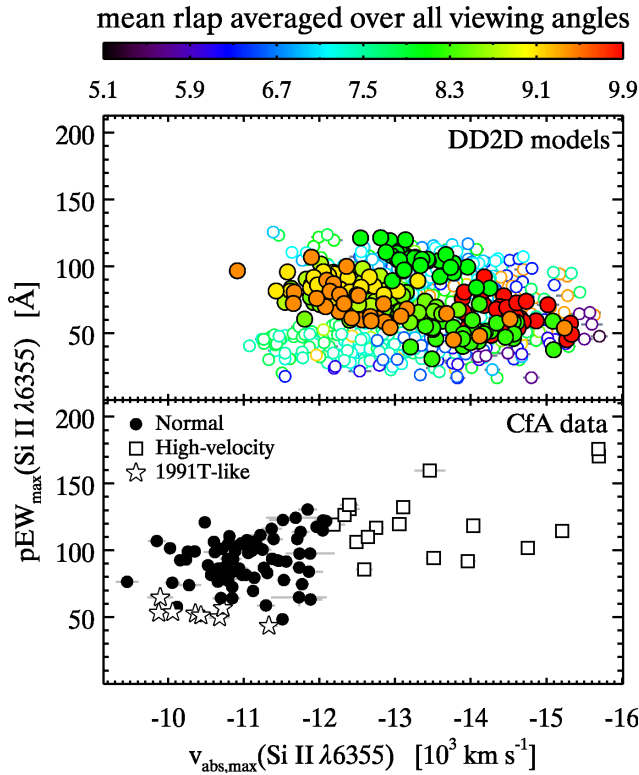


Figure 16. Pseudo-equivalent width of the Si II $\lambda 6355$ line vs. its absorption velocity at maximum light. The colour-coding is the same as in Fig. 9. The symbols for the data points correspond to the spectroscopic subclasses defined by Wang et al. (2009a).

responding to the largest extent of the ^{56}Ni distribution. For models with a symmetric distribution of ^{56}Ni , one expects the expansion rate to scale approximately with $\sqrt{E_{\text{kin}}/M}$. Fig. 16 shows that one of our selected models with the lowest kinetic energy (DD2D_iso_06_dc5, filled yellow circles; $E_{\text{kin}} \approx 1.3 \times 10^{51}$ erg, see Table 1) has lower $|v_{\text{abs}}|$ than one of our selected models with the highest kinetic energy (DD2D_iso_03_dc1, filled red circles; $E_{\text{kin}} \approx 1.5 \times 10^{51}$ erg). To see whether this holds for the other 2D models of KRW09, we show the relation of $v_{\text{abs,max}}(\text{Si II } \lambda 6355)$ vs. kinetic energy in Fig. 17.

We do not see a general trend of increasing $|v_{\text{abs}}|$ with kinetic energy, although the models with the highest mean absorption velocity all have $E_{\text{kin}} > 1.45 \times 10^{51}$ erg. The lack of a general trend may seem contrary to expectations, but it reflects the impact of the different distributions of ignition points in each model series on the distribution of intermediate-mass elements in the ejecta. Within a given model series (i.e. for a given ignition setup), the mean $|v_{\text{abs}}|$ increases with the kinetic energy of the explosion, which is directly related to the criterion for deflagration-to-detonation transition (E_{kin} decreases steadily from dc5 to dc1 within a model series; see Table 1). We illustrate this for the DD2D_iso_06 model series in Fig. 17 (dotted line).

In a recent paper, Foley & Kasen (2011) noted a correlation between the Si II $\lambda 6355$ absorption velocity at maximum light with $B^{\text{max}} - V^{\text{max}}$ pseudo-colour⁶ at the same age, redder SNe Ia having higher $|v_{\text{abs}}|$. The lower panel of Fig. 18 shows the relation of

⁶ difference between the B magnitude at B -band maximum and the V magnitude at V -band maximum.

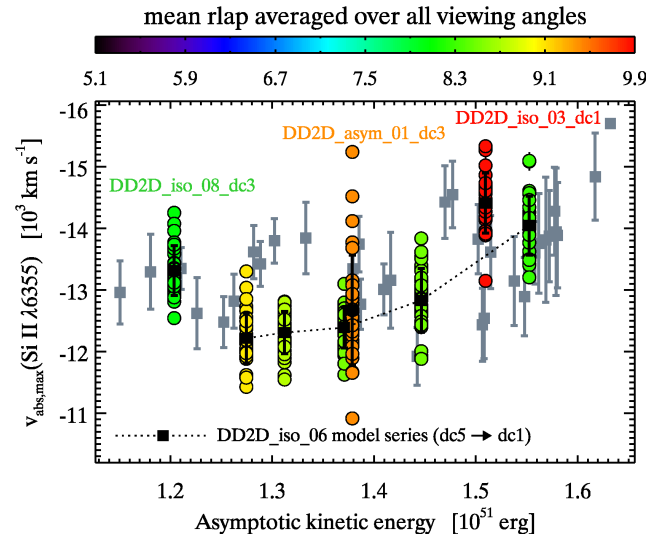


Figure 17. Absorption velocity of the Si II $\lambda 6355$ line at maximum light vs. asymptotic kinetic energy. The colour-coding is the same as in Fig. 9. For our subset of selected models (filled circles), we show the complete set of 30 measurements (one per viewing angle). For all other models, only the mean v_{abs} and its standard deviation (grey squares) are plotted. Last, the dotted line corresponds to the relation of $v_{\text{abs,max}}(\text{Si II } \lambda 6355)$ with kinetic energy for the DD2D_iso_06 model series.

$v_{\text{abs,max}}(\text{Si II } \lambda 6355)$ with intrinsic $B - V$ colour at B -band maximum (as opposed to $B^{\text{max}} - V^{\text{max}}$ pseudo-colour) in data from the CfA SN Program. Although the correlation between both quantities is rather weak ($r = -0.37$; but note the large error on intrinsic $B - V$ colour), the slope of the relation is in agreement with that found by Foley & Kasen (2011). For the 2D models of KRW09 (Fig. 18, upper panel), the general trend is in the opposite direction (dashed black line). Within each model, the trend of absorption velocity with colour generally also has the opposite trend as that seen in the data.

Foley & Kasen (2011) provide a simple explanation for the observed correlation by invoking the greater line opacity in the B -band for SNe Ia with high-velocity ejecta, both through increased line overlap and a greater impact of Fe II/Co II lines in the outer cooler regions of the ejecta where higher-velocity spectral features are formed. Based on radiative transfer calculations by Kasen & Plewa (2007), they show that the detonating failed deflagration (DFD) model of Plewa (2007) is consistent with the association of redder $B - V$ colour with larger Si II $\lambda 6355$ blueshifts, when viewed from different viewing angles. As mentioned earlier, the 2D models of KRW09 also display variations of the Si II $\lambda 6355$ absorption velocity with viewing angle, with associated variations in $B - V$ colour, but the correlation in most cases is in the opposite direction as that seen in the DFD model, and in all cases much weaker than shown by Foley & Kasen (2011) (their Fig. 8). Since the radiative transfer code used by KRW09 and Kasen & Plewa (2007) is the same, this discrepancy must be traced back to differences in the explosion models (whether intrinsic or resulting from different physical approximations and numerical treatment thereof) or nucleosynthetic post-processing (Kasen & Plewa 2007 used an approximate alpha-network scheme which for instance does not include sodium, while KRW09 used a more elaborate nuclear network to compute detailed abundances for a representative model, and interpolated the output for all other models). Analysis of more DFD models would be needed to check whether the correlation be-

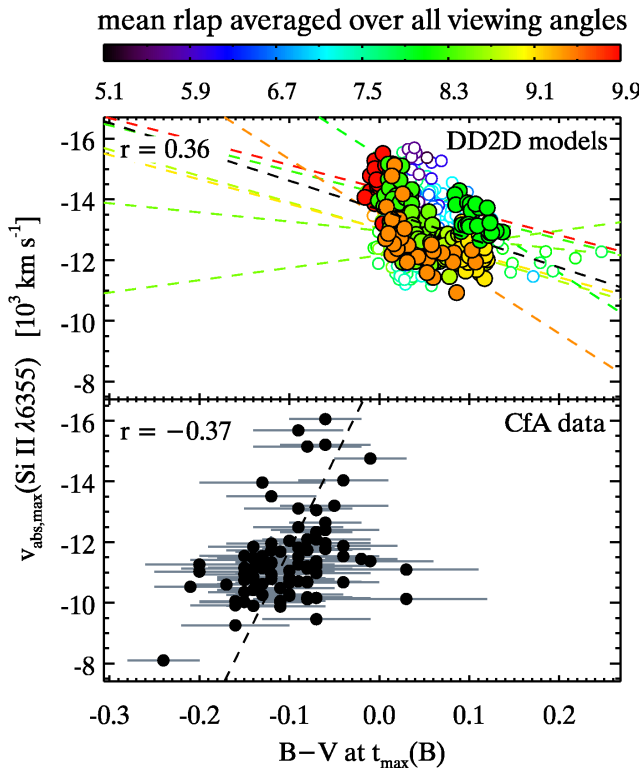


Figure 18. Absorption velocity of the Si II $\lambda 6355$ line at maximum light vs. intrinsic $B - V$ colour at B -band maximum, in the 2D models of KRW09 (upper panel) and in data from the CfA SN Program (lower panel). The colour-coding is the same as in Fig. 9. In both cases, we show a linear fit to the entire sample (dashed black line) and report the Pearson correlation coefficient (r) of $v_{\text{abs,max}}$ with intrinsic $B - V$ colour. We also show the linear relations obtained from fits to individual models (dashed colour lines).

tween Si II $\lambda 6355$ absorption velocity and maximum-light $B - V$ colour is a generic feature of this type of explosion. This is apparently not the case for delayed-detonation models of SNe Ia, although Fig. 18 once again shows that the 2D models of KRW09 lie in a different region of parameter space than the data (larger Si II $\lambda 6355$ blueshifts and redder $B - V$ colours).

One possible explanation resides in the different distributions of iron-group and intermediate-mass elements in both DFD and delayed-detonation models. In the DFD model, the deflagration is ignited on one side of the ejecta, but detonates on the opposite side, causing both IGE and IME to be ejected at high velocities on the ignition side. In delayed-detonation models, the IGE and IME are preferentially ejected in opposite directions (see Fig. 1, *bottom row*). Since the distribution of IGE sets the $B - V$ colour to a large extent (see, e.g. Kasen & Woosley 2007), one might expect the two detonation models to show opposite trends for $|v_{\text{abs}}|$ and $B - V$.

5.2 Spectral evolution

The comparison of maximum-light spectral properties in the previous section has several practical advantages: more data are available at this age and they are of better quality (the use of a Monte Carlo radiative transfer code means this is also true of the model spectra, which consist of a higher number of photon packets at maximum light). Any thorough validation of a SN Ia model should, however, include a comparison of the time evolution of its spectra

with observations. As the supernova expands, the layers where the spectrum is formed recede to deeper regions of the ejecta, where the composition is different and the expansion velocity smaller. By measuring various parameters of individual spectral features and their evolution with time, one has a complete census of a model’s failures and successes: a poor model might reproduce certain spectral features at certain times, but a good model should reproduce *all* features at *all* times.

5.2.1 Overall evolution

In Fig. 19 we show the spectral evolution of model DD2D_iso_06_dc2 viewed along $\theta = 88^\circ$ (see Fig. 3 for the corresponding $UBVRIJHK_s$ light curves), in five-day increments between -10 and $+20$ d from B -band maximum (i.e. between ~ 10 d and ~ 40 d past explosion), compared to observations of SN 2003du. Both models and observations correspond to a SN Ia with $\Delta m_{15}(B) \approx 1$.

At -10 d, the model spectrum displays a much bluer (hotter) SED with weaker features than SN 2003du. The absorption due to Ca II H&K ($\sim 3700 \text{ \AA}$) is much weaker, and that due to the Ca II IR triplet ($\sim 8000 \text{ \AA}$) is non-existent, both clear signs of over-ionization in the ejecta. The weak Ca II H&K line certainly contributes to the excess of U -band flux inferred from comparisons of $U - B$ colour curves (Fig. 12), but most of the discrepancy appears to originate blueward of this, in a region dominated by absorption by iron-group elements (*grey highlighted region*). This is most clearly seen in the $+5$ d spectrum of SN 2003du, which unlike the earlier ones extends blueward of 3600 \AA . As noted earlier based on the $U - B$ colour curves, this excess of U -band flux remains important up until $+5$ d, at which point the absorption due to Ca II H&K has significantly strengthened in the models though remains weaker than in SN 2003du. The S II doublet ($\sim 5400 \text{ \AA}$), well fit at -5 d is too weak in the models between $+0$ d and $+10$ d. The same is true of the two iron-group dominated absorption complexes at $\sim 4300 \text{ \AA}$ and $\sim 4800 \text{ \AA}$, which also reveal some of the model shortcomings from maximum light onwards. The velocity offset in the Si II $\lambda 6355$ absorption (broader yet shallower in the models; *red dotted line*) also becomes apparent at maximum light. Interestingly, the Si II $\lambda 6355$ absorption velocity appears to remain almost constant between -10 d and $+10$ d while it decreases steadily in SN 2003du.

From $+10$ d onwards, we highlight several discrepancies in other wavelength regions. The model appears to lack an absorption around $\sim 5000 \text{ \AA}$, which in SN 2003du and other SNe Ia is part of a complex Fe II/Co II absorption feature. The pseudo equivalent width of this feature at $+10$ d is systematically $\sim 50 \text{ \AA}$ smaller in all the models with respect to observations. It is difficult to disentangle the effects of temperature (if too hot, as clearly the case before maximum light, this would delay the III \rightarrow II recombination timescale of iron-group elements), the impact of the LTE approximation (non-LTE effects are particularly important in treating the Fe II/Co II opacities; see Baron et al. 1996), and the high ejecta velocities (as clearly seen from the large blueshift of the Ca II IR triplet absorption)– which would enhance line overlap and smear out small-scale absorption features.

Another striking feature is the lack of emission in the model around 5800 \AA . This feature is commonly attributed to the Na I D doublet. The absence of a strong 5800 \AA feature is a generic feature of these models, and not just particular to model DD2D_iso_06_dc2. The radiative transfer calculations we have at our disposal do not extend beyond $+25$ d or so past B -band maximum, so we cannot

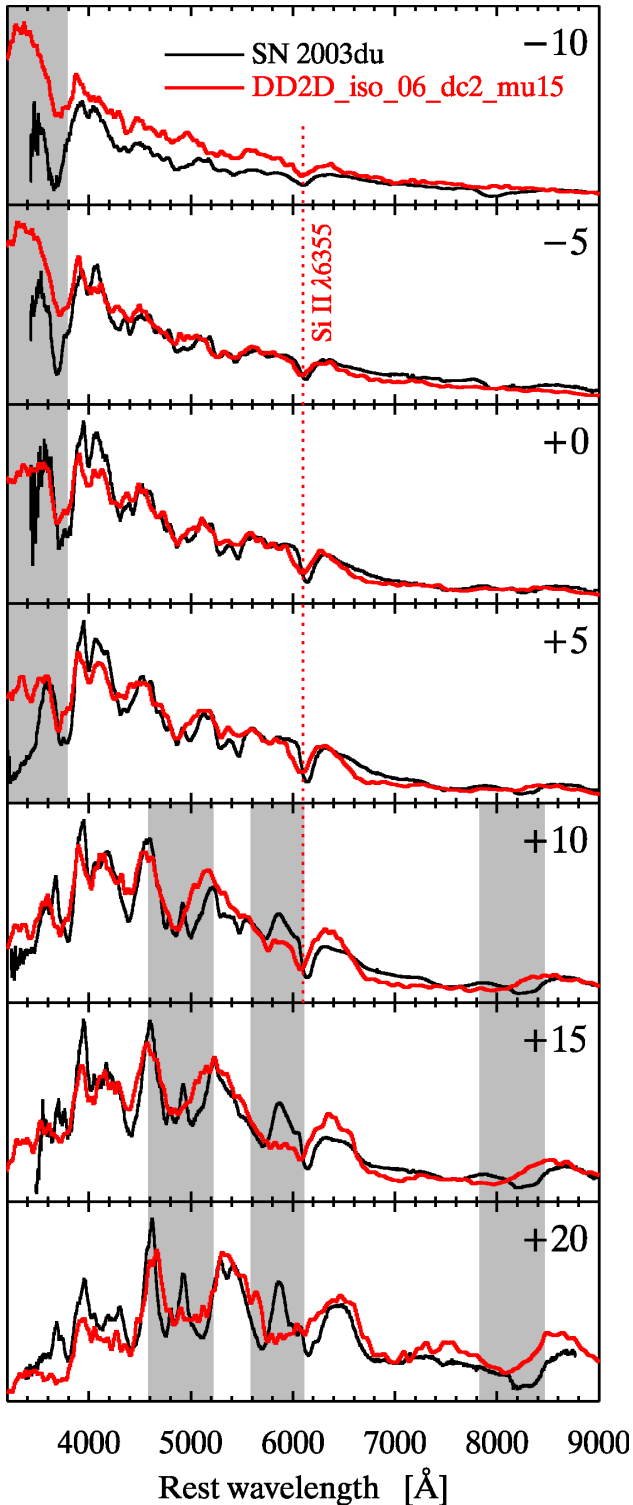


Figure 19. Spectroscopic evolution of model DD2D_iso_06_dc2 viewed along $\theta = 88^\circ$ (red), compared to spectra of SN 2003du (black; Anupama, Sahu & Jose 2005; Stanishev et al. 2007). The synthetic and observed spectra have been scaled to match their respective rest-frame absolute B -band magnitude (see Fig. 3). The age of each spectrum is indicated in days from B -band maximum in the top-right corner of each plot. The grey shaded regions highlight the model U -band excess (between -10 d and $+5$ d), and several disagreements around 5000 \AA , 5800 \AA , and 8200 \AA (respectively attributed to Fe II/Co II, Na I, and Ca II) from $+10$ d onwards. The vertical red dotted line indicates the wavelength location of maximum absorption in Si II $\lambda 6355$ in the models, which remains almost constant between -10 d and $+10$ d.

say whether this line appears at later ages once the ejecta have cooled down, although KRW09 present synthetic spectra of model DD2D_iso_06_dc2 at $+31$ d that do not show evidence for this feature (their Fig. 2). Artificially removing this line in the spectra of SN 2003du can lead to R -band magnitude differences of up to ~ 0.2 mag, and could explain part of the discrepancy in $B - R$ and $V - R$ colours between models and observations past maximum light (see Fig. 12).

Non-LTE calculations by Baron et al. (2006) fail to reproduce this feature (their Fig. 4), so the LTE approximation used by KRW09 is not necessarily the cause of this discrepancy. If this line is Na I D, the LTE approximation should be able to partly reproduce this strong resonance line if sodium is abundant in its neutral stage ($X_{\text{Na}} = 10^{-5}$ throughout the ejecta in all the models of KRW09, roughly corresponding to one third of the solar value; e.g., Asplund et al. 2009). The absence of this line would then be related to an ionization problem (Na I has a low ionization potential of ~ 5.1 eV), which would likely persist until later times due to nonthermal ionization in the ever-thinning ejecta (e.g., Kozma et al. 2005). Another possibility is that this feature is not due to Na I, since its presence is difficult to reconcile with the presence of singly- and doubly-ionized species, but we do not explore this possibility further at this stage.

5.2.2 Absorption velocities

Studying the blueshifts of individual absorptions and their evolution with time enables one to indirectly probe the dynamics of the expansion. As a general rule, the blueshift decreases with time (as does $|v_{\text{abs}}|$), since the spectra form in deeper layers of the ejecta (i.e. at lower mass coordinate) as the SN expands. Various inhomogeneities and radiative transfer effects can, however, affect this simple picture. For example, Quimby, Höflich & Wheeler (2007) invoke a shell-like density structure (formed within the context of a pulsating delayed detonation or WD-WD merger scenario) to explain the ~ 10 -d-long plateau in absorption velocity of the Si II $\lambda 6355$ line in SN 2005hj. As for radiative transfer effects, Dessart et al. (2011) recently showed how taking into account time-dependent terms in the gas energy and statistical equilibrium equations can lead to an *increase* of the He I $\lambda 10830$ blueshift with time (contrary to all other He I lines) in the context of Type Ib/c supernovae.

In what follows we explore the evolution of the absorption velocities in two strong lines in SN Ia spectra: Ca II $\lambda 3945$ (i.e. Ca II H&K) and the characteristic Si II $\lambda 6355$. The Ca II line profile spans a wavelength region where the dominant source of opacity is due to bound-bound transitions (see, e.g. Pinto & Eastman 2000b), and line overlap is an issue (see also Blondin et al. 2006). Moreover, observations of the Ca II IR triplet in early-time spectra of SNe Ia have revealed the presence of high-velocity absorption components (see Mazzali et al. 2005). In what follows, and in the presence of Ca II $\lambda 3945$ profiles with multiple absorptions, we report the velocity associated with the *deepest* absorption. The Si II $\lambda 6355$ line is less affected by line overlap (at least until $+10$ d or so past B -band maximum), although some SNe Ia appear to have a high-velocity component associated with this line at early times (e.g., SN 2005cf; Garavini et al. 2007; Wang et al. 2009b).

In the top row of Fig. 20 we show the evolution of the Ca II $\lambda 3945$ absorption velocity, for four of our selected models (where we have again chosen model DD2D_iso_06_dc2 as representative of the DD2D_iso_06 model series), colour-coded according to viewing angle. The lower panel in each case shows simi-

lar measurements on SNe Ia in the same $\Delta m_{15}(B)$ range from our spectroscopic sample, where the colour-coding is used to distinguish individual supernovae. The models exhibit a strong diversity in absorption velocity evolution. Model DD2D_iso_03_dc1 has a steeply decreasing $|v_{\text{abs}}|$ between -15 d and -5 d from B -band maximum (from 25000 km s^{-1} to 15000 km s^{-1}), and little to no variation at later times. Such a variation is also apparent in some observed SNe Ia, although others display a steadier decrease in $|v_{\text{abs}}|$ beyond $+10$ d. Model DD2D_iso_06_dc1 (*not shown*; $0.85 \leq \Delta m_{15}(B) \leq 1.08$) has a similar behaviour. The other models of the DD2D_iso_06 series, however, all display little variation in the Ca II absorption velocity between -15 d and nearly $+10$ d, with a sharp $\sim 5000 \text{ km s}^{-1}$ drop in $|v_{\text{abs}}|$ around $+10$ d, followed by a second phase of almost no variation. The discontinuous jump in Ca II absorption velocity could be in part related to a measurement artefact due to overlap and changes in relative strength between Si II $\lambda 3858$ and Ca II $\lambda 3945$. The same overall pattern is visible in model DD2D_iso_08_dc3, but it is not present in the data. Interestingly, model DD2D_asym_01_dc3 appears to display both types of behaviour, depending on the viewing angle.

As noted earlier, the Si II $\lambda 6355$ line is far less prone to measurement uncertainties, and is a better probe of the ejecta dynamics than Ca II $\lambda 3945$. The bottom row of Fig. 20 shows the evolution of the Si II $\lambda 6355$ absorption velocity in the same four models, again compared to observations in the same $\Delta m_{15}(B)$ range. Apart from model DD2D_iso_08_dc3, which displays little variation in $|v_{\text{abs}}|$ between -15 d and maximum light, and a steady decrease thereafter, the other three models show almost no variation for a given viewing angle (as expected, the largest scatter at any given age occurs in model DD2D_asym_01_dc3). Models DD2D_iso_03_dc1 and DD2D_iso_06_dc2 even display a slight *increase* of $|v_{\text{abs}}|$ with time. For most models we were unable to reliably measure the location of maximum absorption in Si II $\lambda 6355$ past $+15$ d or so.

Also noticeable are the apparent lack of correlation between the Si II and the Ca II absorption velocities, as well as the absence of high $|v_{\text{abs}}|$ measurements before -10 d. Several SNe Ia from our spectroscopic sample display $\sim 20000 \text{ km s}^{-1}$ blueshifts at early times, where the models seem constrained to $|v_{\text{abs}}| \lesssim 15000 \text{ km s}^{-1}$. Thus, while all the models are consistent with the “high-velocity” subclass of Wang et al. (2009a) based on the Si II $\lambda 6355$ absorption velocity at maximum light (see Fig. 16), they would be considered “normal” when considering the same measurement at -10 d.

5.2.3 Physical interpretation and constraints on models

Within the DD2D_iso_06 model series, model dc1 shows a steady *increase* of $|v_{\text{abs}}(\text{Si II } \lambda 6355)|$ with time, model dc2 shows almost no variation, and models dc3 through dc5 display a pre-maximum plateau followed by a progressively steeper post-maximum decline (Fig. 21, *right*). The post-maximum velocity gradient is in the range $50\text{--}150 \text{ km s}^{-1} \text{ day}^{-1}$ for these latter models, which represents a sizeable fraction of the range of velocity gradients observed by Benetti et al. (2005). The dc1 through dc5 sequence corresponds to decreasing asymptotic kinetic energy within a model series (see Table 1), which directly affects the amount and radial distribution of intermediate-mass elements.

The left panel of Fig. 21 shows the angle-averaged silicon mass density profiles ($= \rho X_{\text{Si}}$) for the dc1–dc5 models of the DD2D_iso_06 model series. Models with higher kinetic energy have a Si density distribution which peaks at higher velocities ($\sim 14000 \text{ km s}^{-1}$ for model dc1 cf. $\sim 7000 \text{ km s}^{-1}$ for model dc5),

resulting in a higher $|v_{\text{abs}}|$ at any given age (see also Fig. 17). These models also synthesize more ^{56}Ni at the expense of intermediate-mass elements, hence both the height and width of the Si density distribution decrease with increasing E_{kin} . This conditions the strength of the Si II $\lambda 6355$ line and its velocity evolution. In models with higher kinetic energy, the lines are expected to be weaker, owing to the lower peak Si density, and to leave a more transient imprint on the spectra: in model dc1, the Si II $\lambda 6355$ absorption profile is identifiable out to ~ 15 d, while it is clearly visible out to ~ 20 d in model dc5. The narrower Si distributions (with less Si at low velocities) result in a more modest change of the absorption velocity past maximum light: the Si II velocity gradient is almost flat in model dc2, and progressively steeper for models dc3 through dc5. The apparent increase in $|v_{\text{abs}}|$ with time for model dc1 is likely due to the weakness of the Si II line in that model, whose absorption profile is biased by neighbouring lines.

The absence of high-velocity ($|v_{\text{abs}}| \gtrsim 15000 \text{ km s}^{-1}$) measurements in the models at early times is a consequence of the drop in the silicon mass fraction in the outer regions of the ejecta ($v \gtrsim 15000 \text{ km s}^{-1}$). To reproduce the Si II $\lambda 6355$ absorption profile in SN 2002bo, a SN Ia with a large absorption velocity at early times ($v_{\text{abs}} \approx -18000 \text{ km s}^{-1}$ at -13 d), Stehle et al. (2005) infer a homogeneous $X_{\text{Si}} \approx 0.3$ for $v \gtrsim 11000 \text{ km s}^{-1}$. In model DD2D_iso_06_dc2, X_{Si} drops by two orders of magnitude (from ~ 0.3 to ~ 0.001) between ~ 16000 and $\sim 21000 \text{ km s}^{-1}$. The lack of a significant fraction of Si at high velocities in the models of KRW09 naturally accounts for the failure of the models to reproduce the high $|v_{\text{abs}}|$ measurements observed in some SNe Ia, but we note that the nucleosynthetic yields in these low-density regions are subject to a large uncertainty.

The absence of $|v_{\text{abs}}| > 25000 \text{ km s}^{-1}$ measurements for Ca II $\lambda 3945$ is a consequence of the velocity cutoff used when remapping the hydrodynamical output on the 2D cylindrical grid for the radiative transfer calculations (see § 2.1). We do note, however, that a low mass fraction $X_{\text{Ca}} \approx 10^{-5}$ is sufficient to yield a Ca II absorption at the cutoff velocity, illustrating the strength of this doublet.

The distribution of intermediate-mass elements typically extends out to $\sim 20000 \text{ km s}^{-1}$ in the models of KRW09, regardless of the initial distribution of ignition points. However, where almost all models with an isotropic distribution of ignition points have IME down to the centre of the ejecta ($X_{\text{IME}} > 10^{-3}$ at $v \approx 0 \text{ km s}^{-1}$), most of the models with an anisotropic distribution (DD2D_asym) have no IME below $\sim 10000 \text{ km s}^{-1}$, and hence display narrow $5000\text{--}10000 \text{ km s}^{-1}$ “shells” of IME in their ejecta. These IME shells are a direct consequence of the weakness of the deflagration due to its one-sided ignition, resulting in a small pre-expansion and an IME synthesis in a thin outer layer of the ejecta, and are clearly incompatible with the large $> 10000 \text{ km s}^{-1}$ widths of absorption profiles observed in SN Ia spectra. Not surprisingly, 5 of the 6 rejected models (see Table 1) have narrow $\lesssim 5000 \text{ km s}^{-1}$ IME shells in their ejecta.

6 DISCUSSION: ARE ASYMMETRIC IGNITIONS RULED OUT BY OBSERVATIONS?

In section 3.3 we rejected six models that do not yield satisfactory matches to observed SN Ia spectra for some viewing angles. Fig. 22 shows spectra for these models viewed along $\theta = 40^\circ$ at maximum light, compared with observed maximum-light spectra in the same $\Delta m_{15}(B)$ range. The mismatch with observations is

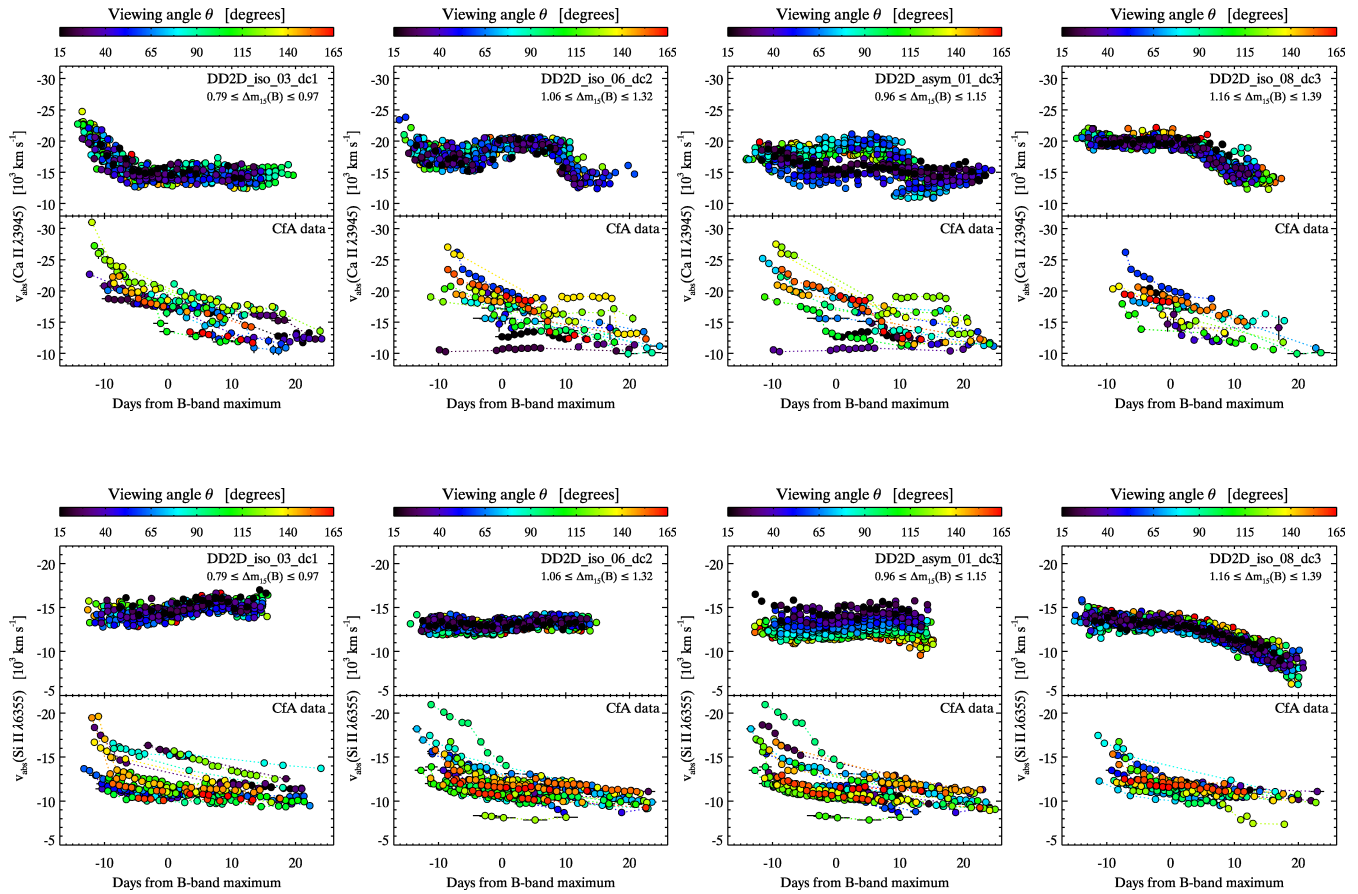


Figure 20. *Top row:* Evolution of the Ca II 3945 absorption velocity with time for four of our selected models (*upper panels*), colour-coded according to the viewing angle θ . The lower panels shows similar curves for SNe Ia in the same $\Delta m_{15}(B)$ range from our spectroscopic sample. The colour-coding in this case denotes individual SNe Ia, whose measurements are connected by dotted lines. *Bottom row:* same as above for the Si II 46355 line.

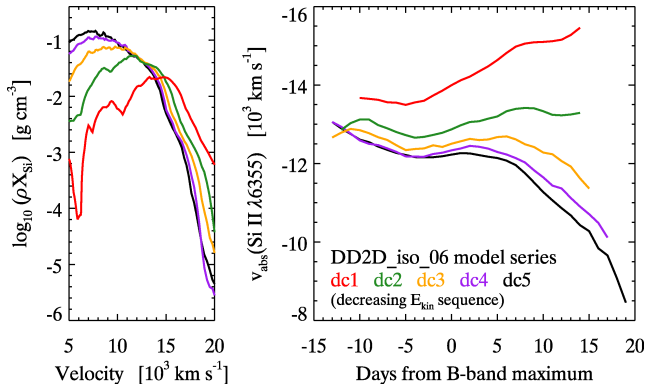


Figure 21. *Right:* Angle-averaged silicon mass density ($= \rho X_{\text{Si}}$) profiles at $t = 100$ s past explosion for the DD2D_iso06 model series (dc1 through dc5). *Left:* Mean absorption velocity curves for Si II 46355 in the same model series.

clear (and these objects would *not* be classified as SNe Ia!⁷, but the synthetic spectra share some common properties: all have a very blue SED characteristic of hot ionized ejecta. Moreover, they show almost no sign of lines from intermediate-mass elements (Ca, S, Si) characteristic of SN Ia spectra, and instead are dominated by

⁷ nor do they yield good matches to SN spectra of other types.

iron-peak elements. This agrees fully with the output from the hydrodynamical simulations: these models have the highest kinetic energy ($E_{\text{kin}} \gtrsim 1.6 \times 10^{51}$ erg) and synthesize the most ^{56}Ni ($M(^{56}\text{Ni}) \gtrsim 1 M_{\odot}$), at the expense of intermediate-mass elements ($M(\text{IME}) \gtrsim 0.15 M_{\odot}$). The association of anisotropic distributions of ignition points with greater amounts of synthesized ^{56}Ni holds for the other DD2D_asym models of KRW09. The deflagration burns less material in these models, and by the time the detonation is triggered, the WD will have expanded less and the burning will occur at higher densities, increasing the fraction of material burnt to nuclear statistical equilibrium, and resulting in a globally symmetric ejecta. A direct observational consequence is that these explosions will tend to yield low $\Delta m_{15}(B)$ values. This is seen in this model series, where the DD2D_asym models have $\Delta m_{15}(B)$ values in a narrow range ($\Delta m_{15}(B) \approx 0.8$), whereas the DD2D_iso models are evenly distributed across $0.9 \lesssim \Delta m_{15}(B) \lesssim 1.4$.

These rejected models may cast some doubts on the validity of the assumption of an anisotropic distribution of ignition points in SN Ia deflagrations. This is in apparent contradiction with the recent study by Maeda et al. (2010a), who associate the observed diversity in the spectroscopic evolution of normal SNe Ia with viewing angle effects in off-center delayed-detonation models. By using nebular lines from stable iron-group elements as probes of the distribution of deflagration ashes (see Maeda et al. 2010b), they showed that SNe Ia displaying low velocity gradients in the

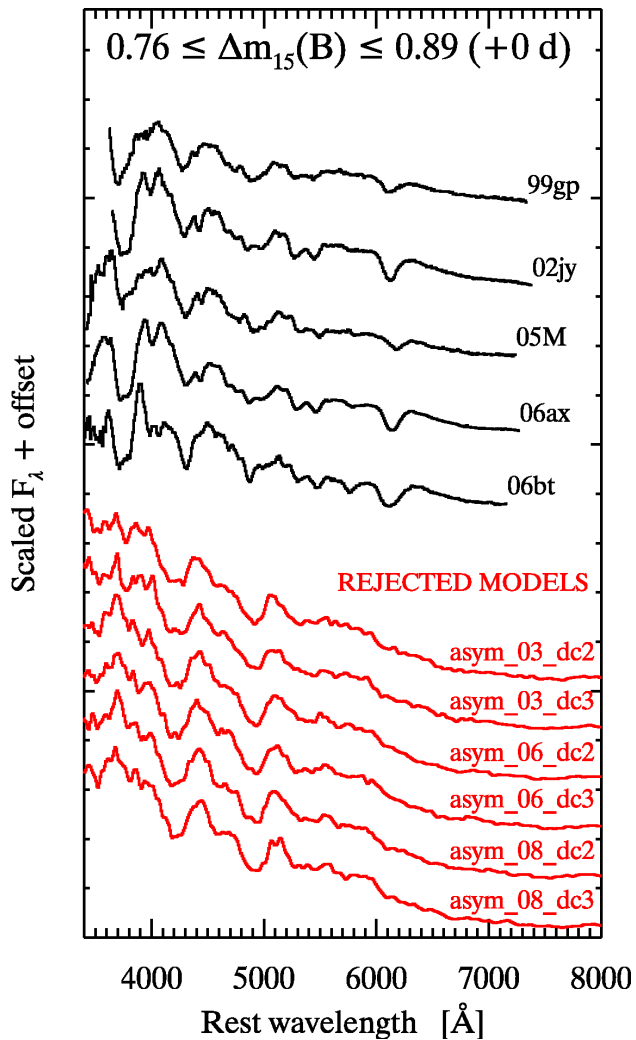


Figure 22. Comparison of observed maximum-light spectra (*black*) with the subset of rejected models viewed along $\theta = 40^\circ$, all in the range $0.76 \leq \Delta m_{15}(B) \leq 0.89$. SN 1999gp and SN 2005M are both 1991T-like SNe Ia.

Si II $\lambda 6355$ line correspond to off-center explosions viewed from the ignition (deflagration) side, while SN with high velocity gradients resulted from the same explosion viewed from the opposite direction.

In the present study, we see a variation of the Si II velocity gradient in explosions with an isotropic distribution of ignition points in which the criterion for deflagration-to-detonation transition is varied. This criterion primarily affects the asymptotic kinetic energy of the explosion and results in a change in the distribution and abundance of silicon in the ejecta (see Fig. 21). While this does not invalidate the interpretation of Maeda et al. (2010a), it nonetheless shows that multiple parameters can affect the steepness of the Si II velocity gradient.

We also note that the most DD2D_asy models of KRW09 yield good matches to observations, such as DD2D_asy_01_dc3 which is part of our subset of selected models. Moreover, not all DD2D_asy models with high explosion energies yield poor matches to observed spectra. Models DD2D_asy_07_dc2 and dc3 have similar properties as the rejected models of Fig. 22, yet their maximum-light spectra are compatible with observed spectra of high-luminosity 1991T-like SNe Ia (see SN 1999gp and SN 2005M

in Fig. 22), and with the peculiar SN 2000cx (Li et al. 2001), both characterized by hot, ionized, and energetic ejecta. Asymmetric ignitions are thus not ruled out as a whole in the present study, but observations suggest that some anisotropic configurations do not occur in Nature.

While the models with an asymmetric distribution of ^{56}Ni result in a larger variation of photometric and spectroscopic properties with viewing angle, we were unable to find *specific* measurements which correlate with the degree of asymmetry in the explosion. Ejecta asymmetries are bound to leave an imprint on the spectral line-profile morphology (see Dessart & Hillier 2011 in the context of Type II supernovae), but such signatures would probably be drowned in Monte Carlo noise in the synthetic spectra studied here. Spectropolarimetric observations of SNe Ia still provide the most direct (yet observationally expensive) probe of ejecta asymmetries (see Wang & Wheeler 2008 for a review), while nebular line profiles offer a means to assess the geometry of the explosion by probing the innermost regions of the ejecta. The limited number of photon packets used in the radiative transfer simulations and the assumption of LTE prevents us to investigate spectropolarimetric signatures or spectra during the nebular phase in the present study.

7 CONCLUSIONS

We have presented a detailed comparison of a recent survey of 2D delayed-detonation explosion models by KRW09 with observations of Type Ia supernovae. We apply standard methods used by SN Ia observers to compare the model light curves and spectra with empirical templates. This represents a significant step forward in the realism of the models. Running several light-curve fitters (MLCS2k2, SALT2, SNooPy) on synthetic (U) BVR I light curves, we find some tension between the light-curve shape of the models and actual data, the models having longer rise times. Based on cross-correlations with a library of SN Ia spectra, we quantified the overall resemblance of individual models to observed SNe Ia, and found that the best models/viewing angles lied systematically on the observed width-luminosity relation.

Comparison of several photometric properties of the models (rise times, maximum-light colours and their evolution with time) shows a broad agreement with observations, but reveals some problems with flux redistribution from the near-UV to the near-IR bands, a key mechanism needed to explain both the width-luminosity relation and the secondary maxima in the NIR light curves, and mediated by the III \rightarrow II recombination timescale of iron-group elements (Kasen 2006; Kasen & Woosley 2007). Subsequent investigation of spectra for a subset of selected models confirmed the excess of U -band flux in the models at early times, likely caused by a hot ionized ejecta and subsequent lack of absorption by Fe II/Co II. Interestingly, one of our selected models (DD2D_iso_08_dc3) that shows the best overall agreement in optical and NIR colour evolution with observations lies off the width-luminosity relation (i.e. the colours match, but not the luminosity). This reveals one limitation of our approach, which relies on maximum-light spectra to rank the different models, whereas a combination of photometric and spectroscopic properties is needed for a proper evaluation.

Comparison of maximum-light spectra show the models have systematically large absorption velocities (most visible in the Si II $\lambda 6355$ line), affecting the relative shapes and strengths of spectral features and smoothing out small substructures observed in iron-dominated absorption complexes at $\sim 4300 \text{ \AA}$ and $\sim 4800 \text{ \AA}$.

Consequently, correlations between several spectroscopic indicators and $\Delta m_{15}(B)$ decline rate have a much larger scatter in the models. The relation found by Foley & Kasen (2011) between Si II $\lambda 6355$ absorption velocity and intrinsic $B - V$ colour (redder SNe Ia having larger $|v_{\text{abs}}|$) is also not reproduced in the models, most showing a weak correlation in the opposite direction. However, the observed correlation is weak and subject to a large uncertainty given the errors on intrinsic $B - V$ colour inferred from the data. Nonetheless, we identify a trend of larger absorption blueshifts for higher kinetic energy for models in which only the criterion for deflagration-to-detonation transition is varied.

The overall evolution of the model spectra compares well with observations, as illustrated by the comparison of synthetic spectra for model DD2D_iso_06_dc2 between -10 d and $+20$ d from B -band maximum with observed spectra of SN 2003du, but several discrepancies characteristic of most models are apparent. The synthetic spectra are too blue (i.e. too hot) at early times, and the ionization that ensues affects their subsequent evolution. Most notably, the models appear to lack an absorption feature around ~ 5000 Å (attributed to Fe II/Co II), and fail to reproduce the strong emission feature at ~ 5800 Å (attributed to Na I D) from $+10$ d onwards. Non-LTE calculations of SN Ia spectra also fail to reproduce this line (Baron et al. 2006).

The evolution of the Ca II $\lambda 3945$ absorption velocity with time exhibits a strong diversity in the models which contrasts with the steady and smooth decrease seen in the data. Model DD2D_asym_01_dc3 has an asymmetric ^{56}Ni distribution and shows all types of behaviour depending on the viewing angle, due to the varying radial Ca distribution with different lines of sight. The evolution of the Si II $\lambda 6355$ velocity shows little variation before maximum light, while the post-maximum evolution (the velocity gradient) appears conditioned by the kinetic energy of the explosion, affecting the abundance and radial distribution of silicon. While this does not contradict the recent findings of Maeda et al. (2010a), who associate the observed diversity in velocity gradients with viewing angle effects in off-center explosions, it shows that the interpretation of such gradients depends on more than a single parameter of the explosion.

We reject six models of KRW09 with highly asymmetric ignition conditions and are characterized by large amounts ($\gtrsim 1 M_{\odot}$) of ^{56}Ni . We do not reject off-center delayed-detonation models for SNe Ia as a whole, but note the extreme sensitivity of the amount and distribution of burning products in the deflagration phase to the initial distribution of ignition points (see also Livne, Asida & Höflich 2005).

Throughout this paper we have focused on discrepancies between the models and observations more than we have highlighted their mutual agreement, but this merely results from the unprecedented level of detail of our study. Such detail is necessary to use the predictive power of the models to provide a physical basis to some observed trends, as well as use the data to impose meaningful constraints on the models. The 2D delayed-detonation models of KRW09 have a degree of fidelity which makes them amenable to the same analysis we use on observations of SNe Ia, but they still require some adjustments to accurately match the data. The ability to reproduce the bolometric/multi-band light curves and the width-luminosity relation is a necessary but not a sufficient condition for a model to be considered a valid approximation of real SNe Ia. Further insights from three-dimensional hydrodynamical simulations, more accurate nucleosynthetic post-processing, and full non-LTE radiative transfer calculations are all part of the solution. We are confident that a detailed comparison of light curves and spectra

from grids of models using the framework developed in this paper will lead to a better understanding of SN Ia explosion mechanisms.

ACKNOWLEDGMENTS

SB acknowledges useful discussions with Luc Dessart, Ryan Foley, Alexei Khokhlov and Masaomi Tanaka. This research has been supported by the DOE SciDAC Program (DE-FC02-06ER41438). Computing time was provided by ORNL through an INCITE award and by NERSC. The work of FKR is supported by the Deutsche Forschungsgemeinschaft via the Emmy Noether programme (RO 3676/1-1). Support for supernova research at Harvard University, including the CfA Supernova Archive, is provided in part by NSF grant AST 09-07903.

REFERENCES

- Anupama G. C., Sahu D. K., Jose J., 2005, *A&A*, 429, 667
 Arsenijevic V., Fabbro S., Mourão A. M., Rica da Silva A. J., 2008, *A&A*, 492, 535
 Asplund M., Grevesse N., Sauval A. J., Scott P., 2009, *ARA&A*, 47, 481
 Baron E., Bongard S., Branch D., Hauschildt P. H., 2006, *ApJ*, 645, 480
 Baron E., Hauschildt P. H., Nugent P., Branch D., 1996, *MNRAS*, 283, 297
 Benetti S. et al., 2005, *ApJ*, 623, 1011
 Bessell M. S., 1990, *PASP*, 102, 1181
 Blondin S. et al., 2006, *AJ*, 131, 1648
 Blondin S., Mandel K. S., Kirshner R. P., 2011, *A&A*, 526, A81+
 Blondin S., Tonry J. L., 2007, *ApJ*, 666, 1024
 Burns C. R. et al., 2011, *AJ*, 141, 19
 Chotard N. et al., 2011, *A&A*, 529, L4+
 Ciotti L., D’Ercole A., Pellegrini S., Renzini A., 1991, *ApJ*, 376, 380
 Cohen M., Wheaton W. A., Megeath S. T., 2003, *AJ*, 126, 1090
 Contardo G., Leibundgut B., Vacca W. D., 2000, *A&A*, 359, 876
 Contreras C. et al., 2010, *AJ*, 139, 519
 Dessart L., Hillier D. J., 2011, submitted to *MNRAS*
 Dessart L., Hillier D. J., Livne E., Yoon S.-C., Woosley S., Waldman R., Langer N., 2011, accepted to *MNRAS*
 Fabricant D., Cheimets P., Caldwell N., Geary J., 1998, *PASP*, 110, 79
 Folatelli G. et al., 2010, *AJ*, 139, 120
 Foley R. J., Kasen D., 2011, *ApJ*, 729, 55
 Foley R. J., Narayan G., Challis P. J., Filippenko A. V., Kirshner R. P., Silverman J. M., Steele T. N., 2010, *ApJ*, 708, 1748
 Gamezo V. N., Khokhlov A. M., Oran E. S., 2005, *ApJ*, 623, 337
 Garavini G. et al., 2007, *A&A*, 471, 527
 Guy J. et al., 2007, *A&A*, 466, 11
 Hayden B. T. et al., 2010, *ApJ*, 712, 350
 Hicken M. et al., 2009, *ApJ*, 700, 331
 Hillebrandt W., Niemeyer J. C., 2000, *ARA&A*, 38, 191
 Höflich P., Khokhlov A., 1996, *ApJ*, 457, 500
 Howell D. A., 2010, *ArXiv e-prints*
 Hoyle F., Fowler W. A., 1960, *ApJ*, 132, 565
 Iben, Jr. I., Tutukov A. V., 1984, *ApJS*, 54, 335
 Jha S. et al., 2006, *AJ*, 131, 527
 Jha S., Riess A. G., Kirshner R. P., 2007, *ApJ*, 659, 122
 Kasen D., 2006, *ApJ*, 649, 939

- Kasen D., Plewa T., 2007, *ApJ*, 662, 459
- Kasen D., Röpke F. K., Woosley S. E., 2009, *Nature*, 460, 869 (KRW09)
- Kasen D., Thomas R. C., Nugent P., 2006, *ApJ*, 651, 366
- Kasen D., Woosley S. E., 2007, *ApJ*, 656, 661
- Kasliwal M. M. et al., 2008, *ApJ*, 683, L29
- Khokhlov A. M., 1991, *A&A*, 245, 114
- Kozma C., Fransson C., 1992, *ApJ*, 390, 602
- Kozma C., Fransson C., Hillebrandt W., Travaglio C., Sollerman J., Reinecke M., Röpke F. K., Spyromilio J., 2005, *A&A*, 437, 983
- Krisciunas K. et al., 2004, *AJ*, 127, 1664
- Leonard D. C., Li W., Filippenko A. V., Foley R. J., Chornock R., 2005, *ApJ*, 632, 450
- Li W. et al., 2001, *PASP*, 113, 1178
- , 2011, *MNRAS*, 412, 1441
- Livne E., Asida S. M., Höflich P., 2005, *ApJ*, 632, 443
- Maeda K. et al., 2010a, *Nature*, 466, 82
- Maeda K., Taubenberger S., Sollerman J., Mazzali P. A., Leloudas G., Nomoto K., Motohara K., 2010b, *ApJ*, 708, 1703
- Mandel K. S., Narayan G., Kirshner R. P., 2011, *ApJ*, 731, 120
- Mandel K. S., Wood-Vasey W. M., Friedman A. S., Kirshner R. P., 2009, *ApJ*, 704, 629
- Matheson T. et al., 2008, *AJ*, 135, 1598
- Mazzali P. A. et al., 2005, *ApJ*, 623, L37
- Meikle P., Hernandez M., 2000, *Mem. Soc. Astron. Ital.*, 71, 299
- Nugent P., Phillips M., Baron E., Branch D., Hauschildt P., 1995, *ApJ*, 455, L147+
- Pastorello A. et al., 2007, *MNRAS*, 377, 1531
- Perlmutter S. et al., 1999, *ApJ*, 517, 565
- Phillips M. M., 1993, *ApJ*, 413, L105
- Pinto P. A., Eastman R. G., 2000a, *ApJ*, 530, 744
- , 2000b, *ApJ*, 530, 757
- Plewa T., 2007, *ApJ*, 657, 942
- Pskovskii I. P., 1977, *Soviet Astronomy*, 21, 675
- Quimby R., Höflich P., Kannappan S. J., Rykoff E., Rujopakarn W., Akerlof C. W., Gerardy C. L., Wheeler J. C., 2006, *ApJ*, 636, 400
- Quimby R., Höflich P., Wheeler J. C., 2007, *ApJ*, 666, 1083
- Riess A. G. et al., 1998, *AJ*, 116, 1009
- , 1999a, *AJ*, 118, 2675
- , 1999b, *AJ*, 117, 707
- Röpke F. K., 2007, *ApJ*, 668, 1103
- Röpke F. K., Hillebrandt W., Niemeyer J. C., Woosley S. E., 2006, *A&A*, 448, 1
- Röpke F. K., Niemeyer J. C., 2007, *A&A*, 464, 683
- Sauer D. N. et al., 2008, *MNRAS*, 391, 1605
- Schlegel D. J., Finkbeiner D. P., Davis M., 1998, *ApJ*, 500, 525
- Stanishev V. et al., 2007, *A&A*, 469, 645
- Stehle M., Mazzali P. A., Benetti S., Hillebrandt W., 2005, *MNRAS*, 360, 1231
- Stritzinger M., 2005, PhD thesis, Technische Universität München,
- Strovink M., 2007, *ApJ*, 671, 1084
- Taubenberger S. et al., 2008, *MNRAS*, 385, 75
- Tonry J., Davis M., 1979, *AJ*, 84, 1511
- Travaglio C., Hillebrandt W., Reinecke M., Thielemann F., 2004, *A&A*, 425, 1029
- Tripp R., 1998, *A&A*, 331, 815
- Truran J. W., Cameron A. G. W., 1971, *Ap&SS*, 14, 179
- Walker E. S. et al., 2010, *ArXiv:1008.2308*
- Wang L., Baade D., Höflich P., Wheeler J. C., Kawabata K., Khokhlov A., Nomoto K., Patat F., 2006, *ApJ*, 653, 490
- Wang L., Wheeler J. C., 2008, *ARA&A*, 46, 433
- Wang X. et al., 2009a, *ApJ*, 699, L139
- , 2009b, *ApJ*, 697, 380
- Webbink R. F., 1984, *ApJ*, 277, 355
- Wood-Vasey W. M. et al., 2008, *ApJ*, 689, 377
- Woosley S. E., 2007, *ApJ*, 668, 1109
- Woosley S. E., Kerstein A. R., Sankaran V., Aspden A. J., Röpke F. K., 2009, *ApJ*, 704, 255

Table 1. Asymptotic kinetic energies, abundances, peak bolometric luminosities and decline-rate ranges for the 44 2D delayed-detonation models of KRW09.

Model	E_{kin} (10^{51} erg)	$M(^{56}\text{Ni})$ (M_{\odot})	$M(\text{stable IGE})$ (M_{\odot})	$M(\text{IME})$ (M_{\odot})	$M(\text{O})$ (M_{\odot})	$M(\text{C})$ (M_{\odot})	$L_{\text{bol,peak}}$ (10^{43} erg s $^{-1}$)	$\Delta m_{15}(B)$	Notes
DD2D_iso_01_dc2	1.548	0.942	0.199	0.215	0.044	0.007	1.921–2.133	0.91–1.03	
DD2D_iso_01_dc3	1.506	0.889	0.194	0.253	0.061	0.011	1.818–2.026	0.99–1.08	
DD2D_iso_01_dc4	1.463	0.832	0.193	0.289	0.078	0.016	not included
DD2D_iso_01_dc5	1.442	0.809	0.192	0.302	0.085	0.019	1.614–1.812	1.07–1.17	
DD2D_iso_02_dc2	1.569	0.901	0.256	0.210	0.034	0.007	1.863–2.172	0.88–1.16	
DD2D_iso_02_dc3	1.515	0.796	0.253	0.298	0.051	0.010	1.563–1.915	0.97–1.25	
DD2D_iso_02_dc5	1.410	0.612	0.241	0.456	0.082	0.016	1.281–1.430	1.15–1.48	
DD2D_iso_03_dc1	1.509	0.799	0.274	0.280	0.045	0.009	1.763–1.850	0.79–0.97	subset
DD2D_iso_03_dc2	1.385	0.584	0.263	0.448	0.097	0.016	1.277–1.357	0.90–1.16	
DD2D_iso_03_dc3	1.288	0.441	0.257	0.548	0.138	0.028	0.925–1.017	1.08–1.33	
DD2D_iso_04_dc1	1.502	0.774	0.275	0.298	0.051	0.011	1.499–1.938	0.77–0.99	
DD2D_iso_04_dc2	1.379	0.562	0.264	0.470	0.095	0.017	0.983–1.519	0.85–1.19	
DD2D_iso_04_dc3	1.263	0.399	0.255	0.583	0.145	0.027	0.633–1.228	1.06–1.38	
DD2D_iso_04_dc4	1.226	0.369	0.252	0.593	0.162	0.033	0.581–1.147	0.99–1.44	
DD2D_iso_05_dc1	1.470	0.718	0.260	0.357	0.060	0.011	1.560–1.594	0.87–1.11	
DD2D_iso_05_dc2	1.333	0.496	0.249	0.530	0.114	0.019	1.111–1.131	1.06–1.22	
DD2D_iso_05_dc3	1.210	0.330	0.237	0.648	0.160	0.033	0.754–0.826	1.21–1.44	
DD2D_iso_05_dc4	1.151	0.293	0.232	0.648	0.189	0.046	0.691–0.725	1.23–1.44	
DD2D_iso_06_dc1	1.552	0.882	0.256	0.227	0.036	0.009	1.859–1.959	0.85–1.08	subset
DD2D_iso_06_dc2	1.446	0.698	0.247	0.378	0.073	0.012	1.443–1.564	1.06–1.32	subset
DD2D_iso_06_dc3	1.371	0.567	0.240	0.485	0.099	0.019	1.151–1.288	1.21–1.48	subset
DD2D_iso_06_dc4	1.312	0.472	0.235	0.561	0.117	0.025	0.972–1.064	1.30–1.53	subset
DD2D_iso_06_dc5	1.275	0.421	0.231	0.599	0.129	0.029	0.896–0.959	1.34–1.57	subset
DD2D_iso_07_dc2	1.282	0.444	0.246	0.556	0.139	0.023	0.867–1.079	1.04–1.24	
DD2D_iso_07_dc3	1.181	0.346	0.238	0.603	0.183	0.039	0.640–0.861	1.18–1.30	
DD2D_iso_08_dc1	1.477	0.719	0.275	0.341	0.060	0.012	1.534–1.767	0.80–1.07	
DD2D_iso_08_dc2	1.302	0.447	0.259	0.549	0.130	0.023	0.930–1.072	1.00–1.38	
DD2D_iso_08_dc3	1.204	0.329	0.250	0.624	0.169	0.035	0.695–0.785	1.16–1.39	subset
DD2D_asym_01_dc2	1.416	0.677	0.224	0.410	0.081	0.015	1.095–1.811	0.93–1.09	
DD2D_asym_01_dc3	1.379	0.644	0.221	0.419	0.103	0.021	0.997–1.696	0.96–1.15	subset
DD2D_asym_02_dc2	1.387	0.614	0.229	0.454	0.096	0.016	1.234–1.451	0.96–1.23	
DD2D_asym_02_dc3	1.252	0.458	0.216	0.558	0.147	0.027	0.886–1.139	1.18–1.38	
DD2D_asym_03_dc2	1.580	0.982	0.234	0.157	0.028	0.006	1.895–2.460	0.79–0.88	rejected
DD2D_asym_03_dc3	1.572	0.965	0.233	0.171	0.031	0.007	1.834–2.426	0.79–0.88	rejected
DD2D_asym_04_dc2	1.577	0.974	0.201	0.190	0.036	0.007	1.722–2.262	0.80–0.91	
DD2D_asym_04_dc3	1.562	0.955	0.198	0.204	0.042	0.009	1.666–2.243	0.81–0.96	
DD2D_asym_05_dc2	1.538	0.939	0.208	0.211	0.042	0.007	1.979–2.054	0.77–1.00	
DD2D_asym_05_dc3	1.508	0.883	0.205	0.253	0.057	0.011	1.876–1.981	0.82–1.06	
DD2D_asym_06_dc2	1.628	1.082	0.221	0.087	0.014	0.003	2.175–2.562	0.78–0.88	rejected
DD2D_asym_06_dc3	1.622	1.068	0.213	0.104	0.019	0.004	2.144–2.537	0.78–0.89	rejected
DD2D_asym_07_dc2	1.579	1.053	0.175	0.144	0.030	0.005	2.192–2.362	0.74–0.94	
DD2D_asym_07_dc3	1.558	1.034	0.170	0.158	0.038	0.008	2.164–2.332	0.76–0.95	
DD2D_asym_08_dc2	1.632	1.103	0.206	0.081	0.014	0.003	2.113–2.586	0.76–0.87	rejected
DD2D_asym_08_dc3	1.617	1.081	0.189	0.113	0.020	0.005	2.043–2.578	0.77–0.89	rejected